



UNIVERSITY OF AMSTERDAM

MSc Physics

Science for Energy and Sustainability

Master Thesis

---

# Grain size effects in transparent conducting metallic nanowire networks

---

*by*

Teresa Ortmann

Stud.nr: 10879013

*June 2016*

*60 ECTS*

*September 2015 - June 2016*

*1<sup>st</sup> Examiner:*

Prof. Albert POLMAN

*Supervisor:*

Dr. Mark KNIGHT

*2<sup>nd</sup> Examiner:*

Prof. Tom GREGORKIEWICZ





## Abstract

Silver nanowire networks can be used as transparent conducting electrodes (TCE) in devices such as solar cells, with the potential to simultaneously surpass the theoretical limits of metal oxides in both optical and electrical performance. Achieving this requires an understanding of how realistic systems, comprised of multicrystalline metals, perform relative to idealized single-crystal networks. We have studied the optical and electrical behavior of Ag nanowire networks with varying grain structures and pitches (300 to 1000 nm) and have investigated the influence of a Ge seed layer. Individual nanowires within the network had widths between 50-120nm. Fabrication was performed using substrate conformal imprint lithography (SCIL), followed by thermal evaporation at varying rates to control grain structure. From x-ray diffraction and four-point-probe measurements, we find that within the limitations of the employed techniques and the number of investigated samples, a faster evaporation rate leads to larger metal grain sizes. This reduces the accompanying sheet resistance due to the reduced number of grain boundaries. Our best conducting Ag network, evaporated at 15 Å/s, has a sheet resistance of 4.1  $\Omega/\text{sq}$  which is one order of magnitude smaller than that of ITO. Optical transparency of 75 – 90% was observed.

This study provides a path for designs including an optimized transparent electrode based on metallic nanowire networks for increased device efficiency and reduced use of material.



---

# Table of Contents

|          |                                                                        |           |
|----------|------------------------------------------------------------------------|-----------|
| <b>1</b> | <b>Introduction</b>                                                    | <b>3</b>  |
| 1.1      | Introduction . . . . .                                                 | 3         |
| 1.2      | Outline . . . . .                                                      | 3         |
| <b>2</b> | <b>Theory</b>                                                          | <b>4</b>  |
| 2.1      | Electrical conductivity and Mayadas-Shatzkes model . . . . .           | 4         |
| 2.2      | Optical conductivity and plasmonic resonances . . . . .                | 5         |
| 2.3      | Influence of processing and fabrication conditions . . . . .           | 6         |
| 2.4      | Preliminary considerations . . . . .                                   | 7         |
| <b>3</b> | <b>Sample design and fabrication</b>                                   | <b>9</b>  |
| 3.1      | Essential fabrication tools . . . . .                                  | 9         |
| 3.1.1    | Thermal evaporator . . . . .                                           | 9         |
| 3.1.2    | Substrate-conformal imprint lithography . . . . .                      | 10        |
| 3.2      | Sample fabrication . . . . .                                           | 11        |
| <b>4</b> | <b>Methods</b>                                                         | <b>13</b> |
| 4.1      | Scanning electron microscopy . . . . .                                 | 13        |
| 4.2      | Grain size/x-ray diffraction . . . . .                                 | 13        |
| 4.3      | Optical conductivity/Integrating sphere . . . . .                      | 16        |
| 4.4      | Electrical conductivity/Four-point probing . . . . .                   | 17        |
| 4.5      | Height/Atomic force microscopy . . . . .                               | 18        |
| <b>5</b> | <b>Results</b>                                                         | <b>20</b> |
| 5.1      | Height . . . . .                                                       | 20        |
| 5.2      | Grain size . . . . .                                                   | 20        |
| 5.3      | Opto-electrical . . . . .                                              | 22        |
| 5.4      | Insights into substrate-conformal imprint lithography . . . . .        | 26        |
| 5.4.1    | Parameters for sample fabrication, calibration of tool & UV solgel . . | 26        |
| 5.4.2    | Master & stamp fabrication . . . . .                                   | 29        |
| <b>6</b> | <b>Discussion</b>                                                      | <b>32</b> |
| <b>7</b> | <b>Conclusion &amp; Outlook</b>                                        | <b>34</b> |



---

# 1 Introduction

## 1.1 Introduction

Transparent conducting electrodes (TCEs) are needed in many devices such as liquid-crystal displays, touchscreens and solar cells which demand simultaneous transparency and charge carrier conductivity. Indium-tin-oxide (ITO) is the most common TCE material and is used as front and back electrodes in amorphous and multicrystalline silicon solar cells [1]. However, drawbacks include scarcity of indium, brittleness [2] which excludes use on organic substrates and high absorption in the blue [3].

Solar cells such as silicon heterojunction cells in which the amorphous Si layer has poor lateral conductivity usually demand a relatively thick transparent conducting front electrode of 100 nm [2]. A 75 nm thick ITO layer is typical for additional use as antireflection coating with a reflection minimum at 600 nm [4]. An alternative to these metal oxides are silver nanowire (Ag NW) networks which are grids of sub-wavelength dimensions. Their positive effect on a solar cell's performance is two-folded: these networks have been shown to make a reduction of the ITO layer possible due to their higher conductivity. This increases the fill factor because of a lower series resistance than a thick ITO layer. It also allows a larger spacing between macroscopic contacts which reduces shading and thereby increases the current of the cell [5]. Theoretically, metallic nanowire networks can simultaneously surpass the performance both optical and electrical, of metal oxides. It is important to understand how realistic, multicrystalline wires perform compared to idealized single-crystal wires. For this, grain size effects are of importance. Silver nanowire networks have been shown to exceed both optical and electrical performance of ITO [6]. They exhibit anomalous transmission due to plasmonic resonances what make them interesting to study and good candidates for replacing ITO and reducing the use of material, especially rare indium.

The aim of this thesis is to investigate the influence of metallization on Ag NW networks for a more realistic assessment of their opto-electrical performance and potential to replace ITO. The influence of evaporation rate on grain size is investigated. For this, the existing fabrication process using substrate-conformal imprint lithography (SCIL) is optimized using the SCIL tooling.

## 1.2 Outline

In chapter 2, theory and preceding findings that motivate the project are presented. In chapter 3, sample design and fabrication using a new technique is described. In chapter 4, characterization methods are described and in chapter 5 experimental results of all methods are presented. The analysis is supported by simulations using the Finite-Difference Time-Domain (FDTD) method and calculations based on the Mayadas-Shatzkes model. Insights into SCIL that were found during optimization are provided in chapter 5.4. In chapter 6 results are further discussed in a broader context and finally in chapter 7 conclusions are drawn and an outlook is given.

## 2 Theory

The performance of nanowire networks is dependent on its electrical and optical properties. The electrical conductivity of metallic nanowire networks differs from that of continuous films due to size effects. At the same time they are plasmonic structures and their optical conductivity is determined by plasmonic resonances that change with dimensions. In the following, the key aspects of the electrical and optical behavior of metallic nanowires are introduced.

### 2.1 Electrical conductivity and Mayadas-Shatzkes model

Compared to bulk materials, thin films exhibit a sheet resistance

$$R_{\text{sh}} = \frac{\rho}{t} \quad (2.1)$$

with  $\rho$ : (bulk) resistivity of Ag and  $t$ : film thickness.

For the investigated geometry of  $N \times N$  wires per array, the sheet resistance is dependent on the dimensions of individual wires

$$R_{\text{sh}} = \frac{N}{N+1} \frac{\rho L}{wh} \quad (2.2)$$

where  $L$  the wire length, equal to network periodicity/pitch, and  $w$  and  $h$  are wire width and height.<sup>1</sup>

For a more realistic description, the influence of grain boundaries has to be taken into account as the resistivity  $\rho$  in Eq. 2.2 does not sufficiently describe electron scattering from grain boundaries.

In thin films where the distance between grain boundaries is smaller than the electron mean free path to other scatterers such as impurities and phonons, the grain-boundary contribution to scattering needs to be taken into account. A model that describes the relation between electrical conductivity of nanoscale metallic films and electron scattering at grain boundaries and at the surface was developed by Mayadas and Shatzkes [7]. Assuming columnar growing grains, i.e. grain size is equal to film thickness, only grain boundaries normal to the film plane are considered which can be described as delta potentials (see Fig. 2.1a). The average distance between grains is Gaussian-distributed and the scattering probability is expressed by a Boltzmann equation. Using perturbation theory, the reduced conductivity due to grains and background scattering  $\sigma_g$  compared to intrinsic scattering  $\sigma_0$  is

$$\frac{\sigma_g}{\sigma_0} = 3 \left[ \frac{1}{3} - \frac{1}{2}\alpha + \alpha^2 - \alpha^3 \ln(1 + 1/\alpha) \right] \quad (2.3)$$

with  $\alpha = \frac{l_0}{d} \frac{R}{1-R}$  where  $l_0$  is the background electron mean free path,  $d$  the average grain diameter and  $R$  the reflection coefficient.

In a further step, the reduction in conductivity due to surface scattering is taken into account

$$\frac{\sigma_s}{\sigma_0} = \frac{6(1-p)}{\pi k} \int_0^{\pi/2} d\phi \int_0^{\pi/2} \frac{\cos(\Theta) \sin^3(\Phi) \cos^2(\Phi)}{H^2} \frac{1 - e^{-kH \cos(\Theta)}}{1 - p e^{-kH \cos(\Theta)}} d\Theta \quad (2.4)$$

<sup>1</sup>Eq. 2.2 assumes rectangular wires. By substituting  $w \cdot h$  by the actual cross sectional area  $A$  the sheet resistance for more realistic, rounded wires can be calculated. For the minimum wire width of  $w = 50$  nm and an extreme radius of curvature of  $0.3 \cdot w$  the deviation from the modeled rectangular wires is  $< 7\%$ . Compared to microscopy techniques that are employed to extract the wire dimensions, this error is negligible.



with  $k = \frac{t}{l_0}$  and  $p$  a specularity parameter that describes the probability of an electron being specularly reflected from the surface and where

$$H = 1 + \frac{\alpha}{\cos(\Theta)\sin(\Phi)}$$

Finally the total resistivity of a thin film  $\rho_f$  is calculated as

$$\frac{\rho_f}{\rho_0} = \frac{\sigma_0}{\sigma_g - \sigma_s} \quad (2.5)$$

Grain boundary scattering was identified as the prevailing mechanism whereas the influence of grain size on surface electron scattering was found to be negligible [7]. This is illustrated by a good data fit with a constant specularity value  $p$  for varying thicknesses.

Fig. 2.1b shows how electrical resistivity due to grain boundary scattering increases with a smaller average distance between grain boundaries  $d$ .

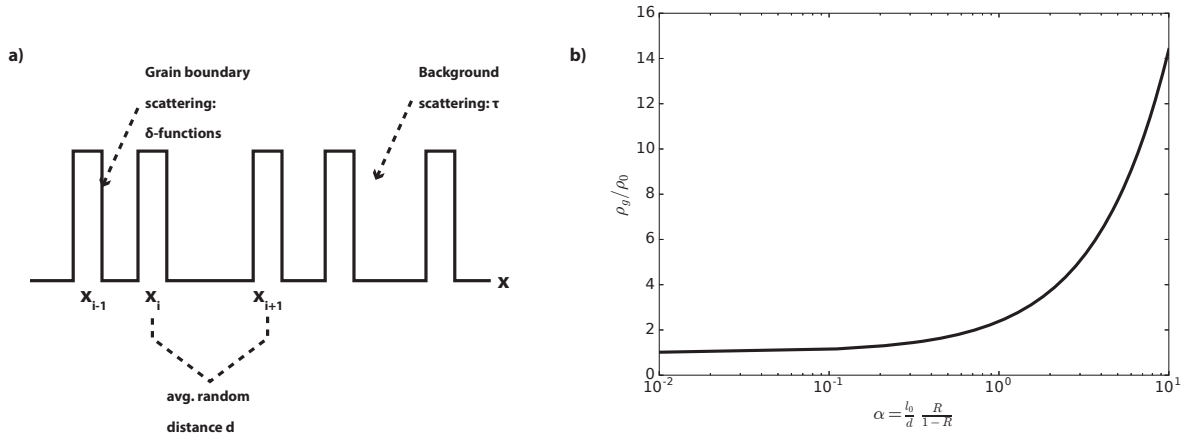


**Figure 2.1:** a) Model for electrical resistivity  $\rho_g$  due to grain boundary and background scattering. Randomly-spaced gaussian-distributed delta-potentials describe grain boundaries perpendicular to the film plane. b) Electrical resistivity due to grain boundary scattering depending on grain size  $d$  according to Eq. 2.3. Based on [7].

## 2.2 Optical conductivity and plasmonic resonances

In the studied design, light can couple to waveguide modes for both linear polarizations and anomalous transmission, which is transmission larger than that of the geometrical cross section, occurs due to scattering from the sub-wavelength features [6]. Metallic sub-wavelength structures support both localized surface plasmon resonance (LSPR) and propagating surface plasmon polariton (SPP).

LSPRs are coherent oscillations of electrons in confined metallic structures and SPPs are waveguide modes that occur at metal/dielectric interfaces and can be coupled to because of the grating geometry. In the studied geometry, for Ag the LSPR occurs at wavelength 450 – 550 nm and the SPP between 750 – 850 nm (for  $\Lambda = 500$  nm).

The spectral position of the SPP strongly depends on wire length because the geometric configuration determines the in-plane momentum which can be transferred. This means only light of a specific wavelength can couple to surface plasmons. The height influences the magnitude of LSPR and SPP resonance as well as the cutoff wavelength of the fundamental

transverse electric  $TE_0$  mode because it affects the cross section interacting with light. With increasing wire width the LSPR becomes more pronounced and red-shifted due to less restoring force whereas the SPP wavelength becomes stronger and blue-shifted due to less confinement in wide wires [6]. This can be observed in FDTD simulations. Fig. 2.2a shows a network with  $\Lambda = 500$  nm and b) with  $\Lambda = 700$  nm. For wavelengths above  $\Lambda$  a step-like increase in transmission occurs that is explained with  $\pm 1$  diffraction orders being directed into the substrate and the collective excitation of LSPRs. The dip in transmission associated with the SPP resonance is not accompanied by a peak in reflection what indicates absorption. By increasing the pitch even more, the SPP resonance can be shifted outside the region of interest ( $> \lambda = 1100$  nm) where silicon cannot absorb due to its bandgap. The small dip in transmission for the  $\Lambda = 700$  nm network at  $\approx 600$  nm is the second order SPP resonance. In Fig. 2.2a a linear decrease in transmission is observed for wavelengths  $> \lambda_{SPP}$ . This feature is ascribed to the cutoff of the  $TE_0$  mode in the metal-dielectric-metal waveguides formed by the wires and air gaps in between [6].

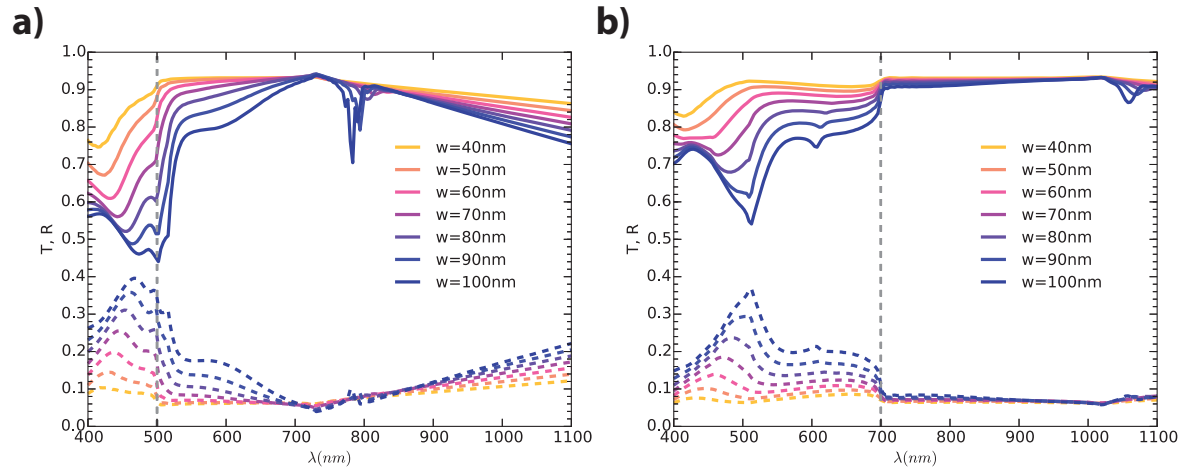


**Figure 2.2:** Transmission and reflection spectra simulated for square Ag wires on  $SiO_2$  with varying widths and a pitch of a) 500 nm and b) 700 nm indicated by the vertical grey dashed lines.

Surface roughness was found to not greatly affect the optical signal of plasmonic nanoparticles. Studies of gold nanoparticles have shown that as long as the aspect ratio is not changed noticeably, the plasmon averages over random height fluctuations. Due to destructive interference the influence on resonances is small [8].

## 2.3 Influence of processing and fabrication conditions

In a comparison between solution-processed and evaporated Ag nanowire networks using the exact same template geometry the MS model was employed to explain better electrical performance that was found for the solution-processed networks [9]. This was ascribed to a larger average grain size and therefore a reduced number of grain boundaries. However, the competing network was evaporated at a slow rate of  $0.5 \text{ \AA/s}$ .

In the fabrication method employed in this thesis metal deposition is performed with thermal evaporation, discussed in Ch. 3.1.1.

Grain growth in thermally evaporated samples happens by surface-diffusion of already deposited atoms into patches [10], [11]. Newly arriving atoms can then either collide with these patches and enlarge them, which is claimed to occur for small evaporation rates or they collide

with each other and form small new nuclei. This is expected to have a higher probability at higher evaporation rates.

Whilst this fundamentally is still valid, more recently it was claimed that in high-vacuum conditions ( $10^{-6} - 10^{-8}$  mbar) for standard plasmonic metals such as Ag the time a sample is exposed to the conditions of a chamber in a thermal evaporator during evaporation is crucial for film quality and grain size due to a relatively high concentration of contaminants such as water vapor and oxygen that can adsorb to the metal film and inhibit further grain growth, called pinning [11]. The quality factor of an optical resonance is described as the ratio of center frequency and width. In the case of LSPR and SPP which occur in metals the Drude parameters plasma frequency  $\omega_p$  and damping constant  $\gamma$  determine their quality [12]. The LSPR and SPP quality factor for Ag, Au, Cu, Al was shown to increase at higher deposition rates compared to values reported in literature obtained for commonly used slower rates [11]. This can be ascribed to the reduced number of electron scattering centers accompanied by a smaller damping constant. Simultaneously this should also have a benefit on electrical conductivity due to less electron scattering, see Eq. 2.3.

Following these paradigms, evaporation at high rates is expected to lead to improved electrical and optical performance of Ag NW networks evaporated in high-vacuum conditions which is competitive with solution-processed networks.

## 2.4 Preliminary considerations

For the studied network geometry, the number of wires  $N$  is very large, between 2000 and 6600 so Eq. 2.2 simplifies. The expected sheet resistance  $R_{sh}$  can then be calculated assuming realistic wire dimensions of  $\Lambda = 500$  nm and  $w = 60$  nm and the bulk resistivity of Ag  $\rho_{bulk} = 1.59 \cdot 10^{-8} \Omega m$  [13]. The results are shown in Table. 1.

| height (nm) | $R_{sh}$ ( $\Omega/sq$ ) |
|-------------|--------------------------|
| 30          | 4.4                      |
| 40          | 3.3                      |
| 50          | 2.7                      |

**Table 1:** Calculated sheet resistances for Ag networks of heights 30 – 50 nm according to Eq. 2.2.

For solar cell application, more significant than the transmission spectra is the value obtained by weighting it with the AM1.5 spectrum. Fig. 2.3 shows FDTD simulations of transmission spectra of wires of the same dimensions as previously and heights of 30 nm (blue), 40 nm (green) and 50 nm (red). Despite the expected shifts (red-shift for the LSPR around 450 nm, blue-shift for the SPP between 900 – 800 nm) and enhanced optical resonances with increasing height (see Ch. 2.2) there is only a small decrease in total transmission of 1% with increasing the height from 40 to 50 nm. The decrease in transmission around  $\lambda = 720$  nm becomes steeper with increasing height because of the larger waveguide cross section.

These results indicate that a wire height of 50 nm will be beneficial as this has a larger positive impact on conductivity than limiting the optical signal.

In the fabrication procedure all six samples should be exposed to the same vacuum conditions for reasons of comparability. Because of this a height larger than 50 nm is not practicable as the raw metal must fit into one evaporation boat.

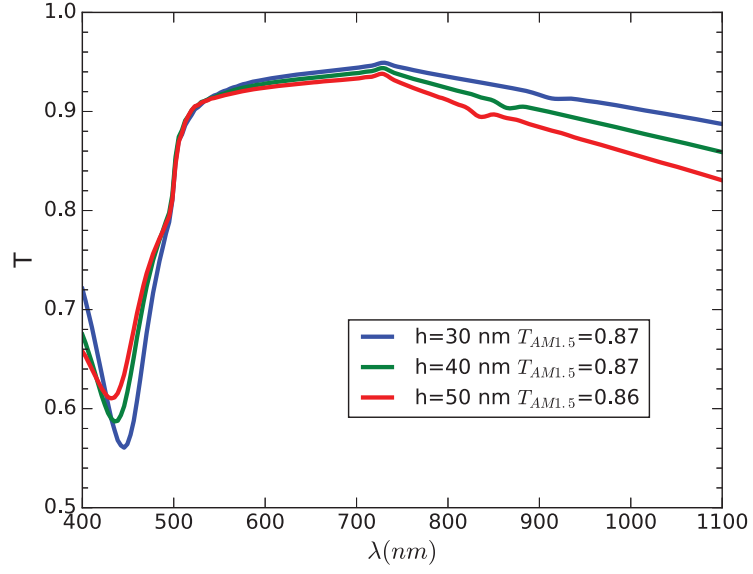


**Figure 2.3:** Transmission spectra and AM1.5-weighted transmission of square Ag NW networks on SiO<sub>2</sub> with pitch=500 nm, width=60 nm and height ( $h$ ) ranging from 30 – 50 nm simulated using *Lumerical's* FDTD method [14].

---

### 3 Sample design and fabrication

The investigated pattern contains 40 nanowire arrays, each  $2 \times 2$  mm, of widths ranging from 50 – 120 nm and periodicities (=pitches)  $\Lambda$  between 300 – 1000 nm, see photograph in Fig. 3.1.

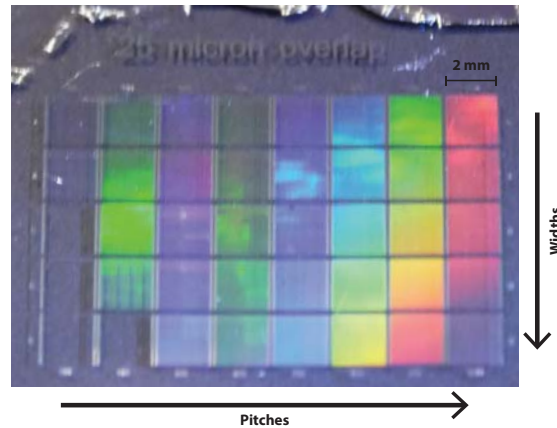


**Figure 3.1:** Photograph of an as-fabricated Ag NW network on a borofloat glass wafer.

#### 3.1 Essential fabrication tools

The operating principles of the thermal evaporator and the imprint tool are introduced, followed by the description of the complete fabrication method.

##### 3.1.1 Thermal evaporator

Thermal evaporation works by heating a source material above its melting point so that the evaporated atoms condense on a substrate. This is done by applying a current to a boat of a material with very high melting point, typically tungsten or molybdenum. It is performed in a high- or ultra-high-vacuum chamber to allow for direct deposition and reduce the amount of residual gases. A schematic of the home-built thermal evaporator used for this project is depicted in Fig. 3.2. The plate on which the samples are mounted and the shutter can be rotated by a motor-driven rod. In the chamber of the thermal evaporator the distance between the metal-filled boat and the sample is shorter than to the quartz crystal microbalance (QCM) which serves as a thickness monitor by detecting changes in the resonance frequency of a quartz crystal due to deposition. For this reason, a geometry factor was determined. This was calibrated by recording height spectra using a *Digital Instruments Dimension 3100* atomic force microscope and comparing it to the displayed value.

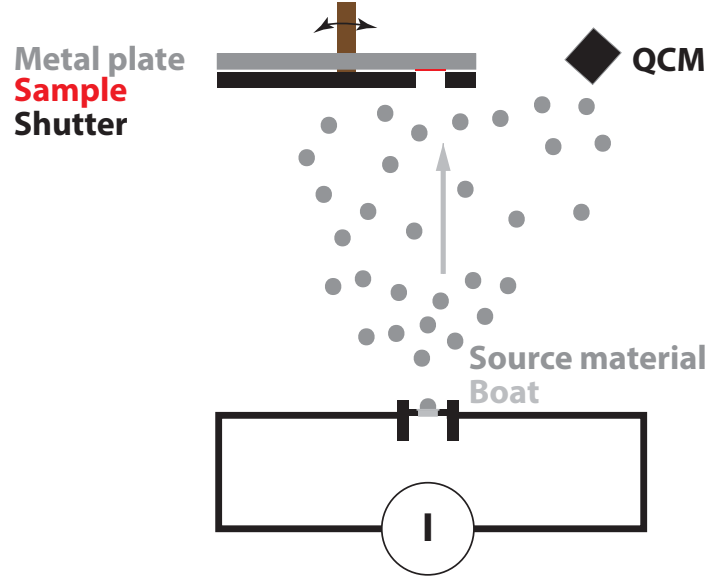


**Figure 3.2:** Schematic of the thermal evaporator chamber consisting of a metal-filled boat connected to a current source, a metal plate on which samples are mounted and a shutter, connected to a motor-driven rod and a QCM to monitor deposited film thickness.

The geometry factor was determined on the basis of scans of two networks each on two samples over a scan length of 4 times the periodicity of 1000 nm. These showed very homogeneous heights and the average was taken for each array, see Table 2. The average of these four conversion factors amounts to 0.64 and was used as calibration factor throughout this thesis.

| QCM display | avg $h$ $\Lambda = 1000$ nm, $w_{\min}$ | avg $h$ $\Lambda = 1000$ nm, $w_{\max}$ |
|-------------|-----------------------------------------|-----------------------------------------|
| 24          | 39                                      | 37                                      |
| 25.5        | 39                                      | 40                                      |

**Table 2:** Thickness displayed on the QCM and heights obtained from AFM scans to calculate a geometry factor for the evaporator.

### 3.1.2 Substrate-conformal imprint lithography

SCIL was the chosen fabrication method as it allows for fast fabrication and good reproducibility of high-resolution nanopatterns. By comparing scanning electron images, the same imprint quality after 3000 imprints was found [15].

SCIL works on the basis of capillary forces between a wafer and a polymer (poly-di-methyl-siloxane, PDMS) stamp. The Young's modulus is a measure of stiffness of solid materials. The stamp is two-layered, with a low Young's modulus PDMS on a glass carrier for conformal contact between the stamp features and the coated wafer and a high modulus X-PDMS layer on top containing the pattern for high resolution and reproducible feature sizes. For use in the SCIL tooling a rubber frame is glued on the glass carrier to hold the stamp by vacuum, see Fig. 3.3.

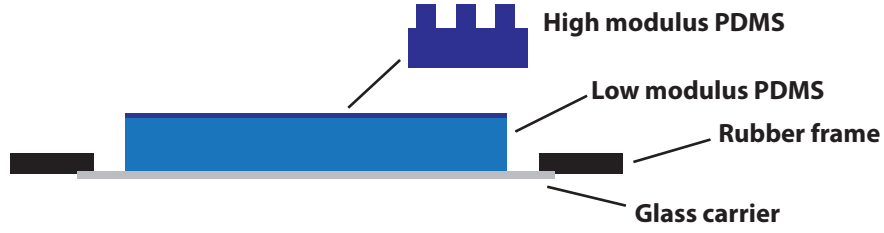


**Figure 3.3:** SCIL stamp consisting of a high Young's modulus PDMS layer containing the pattern, a thicker lower Young's modulus layer and a glass carrier surrounded by a rubber frame.

The SCIL tooling for the Suess mask aligner (*MA 6, Karl Suess*) consists of a stamp holder with vacuum tubes that is connected to a pneumatic cabinet through a pneumatic connector. After loading onto the chuck, the coated wafer is fixed by vacuum and is elevated into a defined process gap (Fig. 3.4a). Then vacuum is successively released from the air tubes (indicated by blue (vertical) lines in Fig. 3.4b and c) to make stepwise contact between stamp and substrate. After the particular exposure and delay time during which the resist is cured, separation occurs by initiating vacuum in the tubes, indicated in orange from the right side in Fig. 3.4d,e. After complete separation (Fig. 3.4f) the chuck is lowered and the wafer can be unloaded after the wafer vacuum is released.

All parameters that can be adjusted are shown in Table. 3 together with the values used for this project.

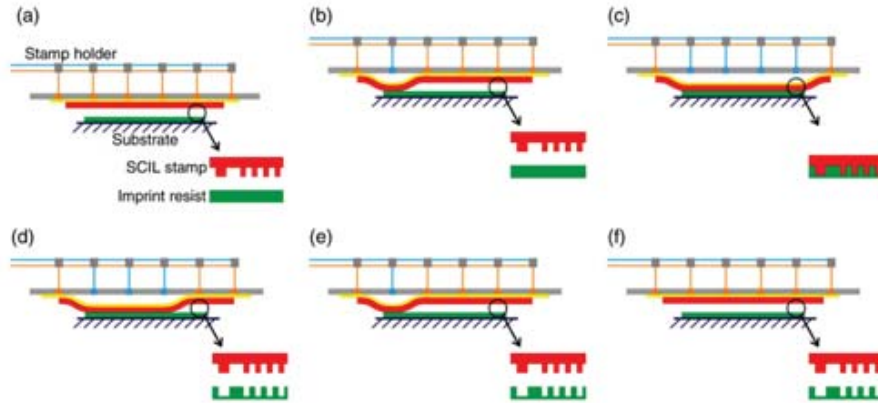


**Figure 3.4:** Imprint sequence in the SCIL tooling. a) coated wafer is brought into process gap, b) stepwise contact between stamp and wafer is made by releasing vacuum from the air tubes in the stamp holder, indicated by the blue on the left side, until c) contact is made over the whole imprint area. d)-f) separation by introducing vacuum in the tubes, beginning from the right until stamp and imprinted substrate are completely separated (taken from [15]).

## 3.2 Sample fabrication

All baking was performed on a hotplate in atmosphere.

2 inch borofloat glass wafers with thickness of 0.7 mm and root-mean-square surface roughness  $< 1$  nm were purchased from *pgo*. As preparation they were ultrasonicated for 5 min in acetone and 1 min in isopropanol to remove organic particles and dust, followed by nitrogen blow-drying. A 1 min pre-bake at  $150^{\circ}\text{C}$  was done to remove moisture. An  $\approx 300$  nm thick layer of PMMA(35k-500) was spincoated (2000 rpm, 45 sec, followed by a 10 min bake at  $150^{\circ}\text{C}$ . A 10 s oxygen reactive ion etch (RIE) (50 sccm, 50 W) was performed to make

---

|                     |                      |
|---------------------|----------------------|
| Process:            | SCIL                 |
| Alignment Gap:      | 100 $\mu\text{m}$    |
| Exposure Time:      | 120 s                |
| WEC Type:           | Contact              |
| WEC-Offset:         | OFF                  |
| Process Delay:      | 60 s                 |
| Process Gap:        | 100 $\mu\text{m}$    |
| Imprint Area:       | 80 mm (for 2" wafer) |
| Exposure:           | ON                   |
| StepTimeImprint:    | 1 s                  |
| StepTimeSeparation: | 0.8 s                |
| Imprint Direction:  | Left                 |
| Release Direction:  | Right                |
| Process Post Delay: | 60 s                 |

**Table 3:** Parameter settings used in the SCIL tool.

the surface hydrophilic. Subsequently a 70 – 100 nm thick layer of silica-based solgel resist (V5-100, purchased from *Philips*) was spincoated (1000 rpm, 10 s) onto the PMMA-coated wafer which was then directly transferred to the SCIL tool (MA6, *Suess MicroTech*). Once in contact with the stamp, solgel curing through UV-exposure was done for 2 min (dose 2.4 J). After a post-bake for 15 min at 70°C RIE was used to first remove the residual solgel in the imprinted trenches (Ar and CHF<sub>3</sub>, 25 sccm each, 67 W for 2:15 min), followed by etching an undercut into the PMMA layer for facilitated lift-off and exposing the glass substrate (50 sccm O<sub>2</sub> for 6 min).

The samples were then loaded into a thermal evaporator (vacuum pressure  $3.0 \cdot 10^{-7}$  mbar) and three samples were evaporated with a 1 nm (rate 0.1 Å/s) seed layer of germanium. Afterwards, 50 nm silver was deposited on all samples and evaporation rates were varied between samples. During evaporation, the rate and thickness was monitored with a QCM.

The lift-off of the PMMA template was performed by soaking in acetone for 10 – 20 min and megasonicing in acetone and isopropanol for 5 – 10 min, removing metal flakes in between by blowing with a syringe.

After x-ray diffraction measurements that require certain sample properties, see Ch. 4.2 were performed, UV-lithography (*MA 6, Karl Suess*) was used to fabricate contact pads that have dimensions of 125  $\mu\text{m} \times 2$  mm and an overlap with the networks of  $\approx 25 \mu\text{m}$ . Each sample was baked for 3 min at 100°C for better adhesion of the HMDS primer (Bis(trimethylsilyl)amine) which was then spin-coated at 4000 rpm in 32 s, followed by a 1 min bake at 100°C.<sup>2</sup> A negative-tone resist (ma-N 1410) was spin-coated (1400 rpm, 32 s), the sample was baked for 90 s at 100°C and then illuminated through a negative foil mask for 18 s (dose 450 mJ), followed by developing in ma-D533s for 85 s and dipping in water twice for 15 s each. Subsequently a 100 nm thick layer of Ag was deposited by thermal evaporation (rate 5 Å/s) followed by the same lift-off procedure as described above.

---

<sup>2</sup>The pre-bake may have a detrimental effect on the Ag NWs as it leads to oxidation which limits conductivity. A test without any pre-bake showed that the exposed pattern exhibited good adhesion after development. However, no metal evaporation of contacts was performed on this test sample and consequently the impact this bake has on conductivity was not studied. This factor can be optimized in further studies.



## 4 Methods

For optical and electrical as well as structural characterization, a multitude of techniques is employed that are presented in the following.

### 4.1 Scanning electron microscopy

Scanning electron microscopy (SEM) provides a good way of imaging subwavelength features by scanning a tightly focused electron beam over a surface which thereby releases secondary electrons. The position-dependent intensity distribution is then captured with a detector and digitally imaged. Brightness depends on to the number of secondary electrons that reach the detector which is related to the electron density in the probed material.

The sample fabrication recipe was tested on a silicon wafer and a FEI Verios SEM was used to obtain high-resolution images and extract the nanosized dimensions of the pattern. The defect-free pattern is shown in Fig. 4.1. The wire width of each network array was obtained by averaging several horizontal and vertical wires.

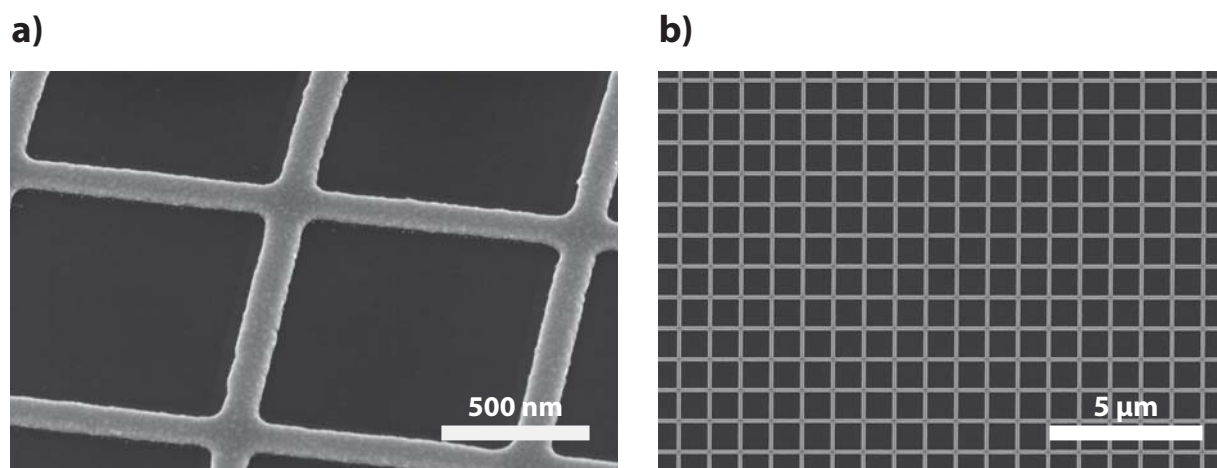


**Figure 4.1:** SEM images of a Ge/Ag network with  $\Lambda = 1000$  nm and  $w = 120$  nm on silicon a) in a  $25^\circ$  tilt and b) in top view.

### 4.2 Grain size/x-ray diffraction

To determine the grain size of evaporated NW networks, x-ray diffraction (XRD) is employed. This technique is based on the diffraction of x-rays on grain boundaries. Diffraction occurs when the Bragg condition

$$n\lambda = 2d\sin(\Theta) \quad (4.1)$$

is fulfilled.

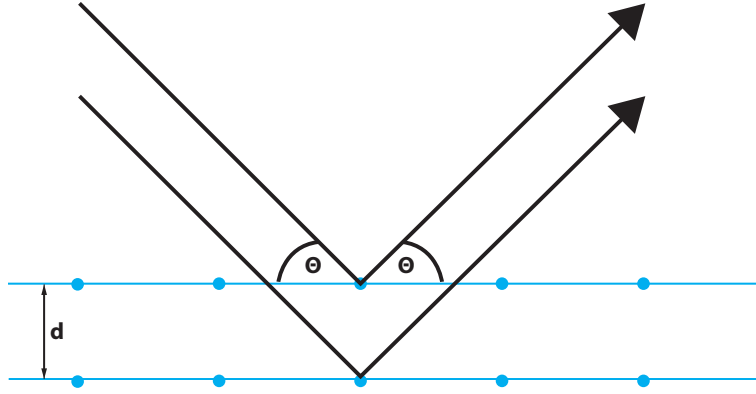


**Figure 4.2:** Bragg diffraction showing two beams of identical wavelength that are diffracted on atoms in different lattice planes in the same angle  $\theta$  when the Bragg condition (see Eq. 4.1) is fulfilled, which means the lower beam travels an additional path of  $d \sin(\theta)$ .

From Fig. 4.2 it is apparent that different grain sizes which can be assumed to be proportional to the number of coherently diffracting planes influence the tolerable angles for constructive interference.

XRD works by illuminating a sample with a monochromatic beam of x-rays. It consists of a goniometer which allows for rotation of sample, source and detector. In the Bragg-Brentano configuration (see Fig. 4.3), which is used for characterization of multicrystalline samples, the sample is tilted by  $\theta$  and the detector tilts by  $2\theta$ . Source and receiving slits are used to focus and collimate, respectively, and a detector for recording the number of diffracted photons per position.

A Bruker D2-phaser in the  $\theta/2\theta$  configuration was used to obtain the number of diffracted x-rays per second at a specific angle  $2\theta$ . A position-sensitive detector (LYNXEYE) was used which does not rotate but records data over 150 positions simultaneously [16]. The source slit was chosen as a circular opening with a diameter of 0.2 mm and a 2 mm slit was positioned above the sample. As the x-ray source copper with a wavelength of  $\lambda = 0.154 \text{ nm } K_{\alpha 1}$  was used and operated at 30keV.

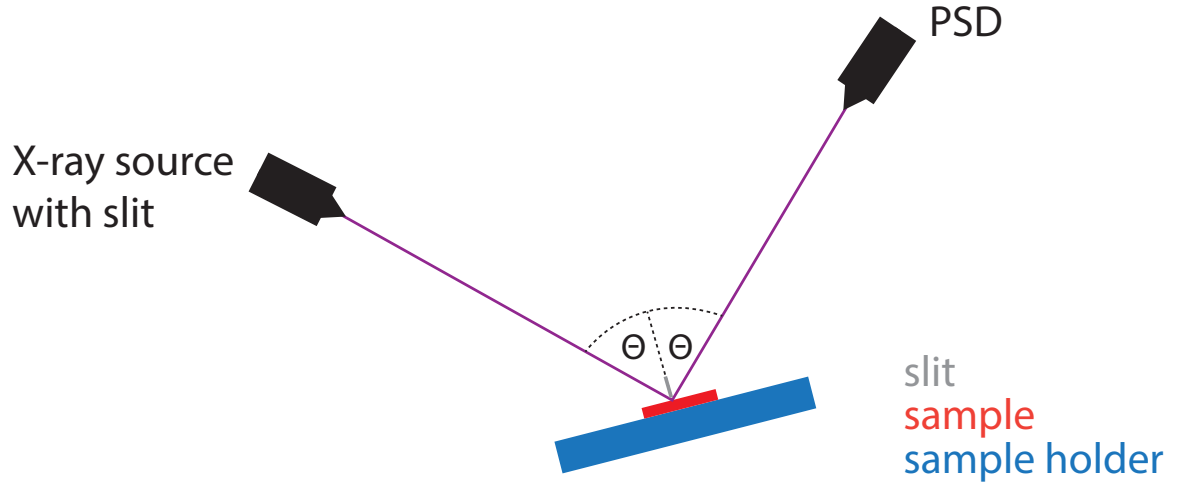


**Figure 4.3:** XRD setup consisting of an x-ray source with slit which focuses the beam onto the sample in an angle  $\Theta$  to the perpendicular. The position-sensitive detector detects the diffracted and by a slit over of the sample collimated beam at the same angle. The sample holder (and in some setups the x-ray source and detector) is connected to a goniometer to control precise angular movements.

The XRD peak width is a measure of grain size as it is inversely proportional to the number of planes contributing to the diffraction under the assumption that strain does not contribute. The most pronounced peak in the samples and therefore considered for analysis is the Ag (111) reflection peak which occurs at a  $2\Theta$  angle between  $38 - 39^\circ$ .

Each spectrum was recorded over an angular range of  $4^\circ$  symmetrically around the peak angle in steps of  $0.01^\circ$  and an integration time of 37 s at each position. This corresponds to a total time of 8 h which yields a high signal-to-noise ratio and least square fit values  $R^2$  between 0.87 and 0.99. The recorded spectra are stripped of  $K_{\alpha 2}$  broadening using the software *Diffac.EVA V3.1* and subsequently they are fitted with a pseudo-Voigt function which is a linear combination of Gaussian G and Lorentzian L

$$V(\Theta) = \eta \cdot L(\Theta) + (1 - \eta) \cdot G(\Theta) \quad (4.2)$$

where  $\eta$  indicates how closely the combination resembles a pure Lorentzian curve. This convolution is traced back to both strain and size distributions that give rise to Gaussian and Lorentzian shape, respectively.

$$G(\Theta) = A_1 \cdot \frac{1}{(\sigma\sqrt{2\pi})} e^{\frac{-(\Theta - \Theta_0)^2}{2\sigma^2}} \quad (4.3)$$

$$L(\Theta) = \frac{A_2}{\pi} \frac{\gamma}{(\Theta - \Theta_0)^2 + \gamma^2} \quad (4.4)$$

with  $A_{1,2}$  the peak amplitudes and  $\sigma$  and  $\gamma$  the peak width parameters of Gaussian and Lorentzian, respectively.

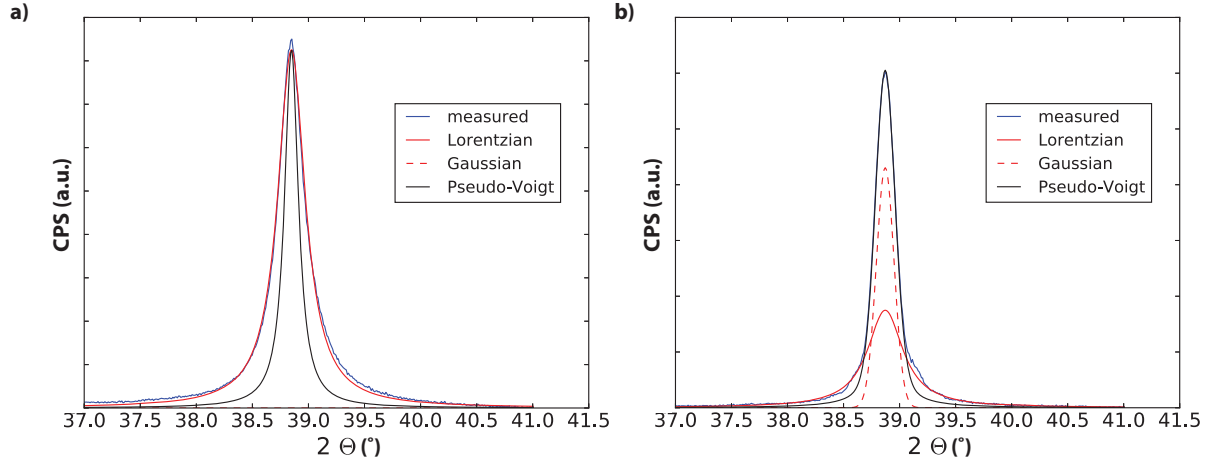


**Figure 4.4:** Spectra obtained with XRD (blue curve), the Pseudo-Voigt fit according to Eq. 4.2 stripped of instrumental broadening according to Eq. 4.5 and Eq. 4.6 (black) and deconvoluted Lorentzian (solid red) and Gaussian (dashed red) for a) a pure Lorentzian ( $\eta = 1$ ) peak shape obtained for a Ge/Ag film on glass and b) a  $\eta = 0.51$  peak shape measured for a Ge film on glass.

The width obtained is corrected for instrumental broadening. For this the XRD peak of a Corundum reference, an  $\text{Al}_2\text{O}_3$  rock with hexagonal structure, occurring at a  $2\theta$  angle of  $35.1^\circ$ , was recorded. This crystal is assumed to have infinitely large grains, which means an infinitely narrow deflection peak and therefore the measured width of  $0.075^\circ$  is ascribed to the instrumental broadening. To correct the fitted Pseudo-Voigt curve for this instrumental broadening the Gaussian and Lorentzian contributions have to be treated differently. For a Lorentzian shape, broadening is described by

$$B_{\text{sample}} = B_{\text{tot}} - B_{\text{instr}} \quad (4.5)$$

whereas for a Gaussian shape

$$B_{\text{sample}} = \sqrt{B_{\text{tot}}^2 - B_{\text{instr}}^2} \quad (4.6)$$

Fig. 4.4 shows a larger broadening effect for more Lorentzian type peaks (large  $\eta$ ). This is expected from Eq. 4.5 as for a narrow peak the subtraction of  $0.075^\circ$  has a larger impact as for Gaussian.

The corrected Lorentzian and Gaussian are then again inserted in the Pseudo-Voigt and then the Full-Width-Half-Maximum (FWHM) is obtained numerically.

In a next step, the grain size can be calculated with the Scherrer equation which can be derived from Eq. 4.1 and correlates a diffraction peak to an average grain size  $L$  [17].

$$L = \frac{K\lambda}{B\cos(\Theta)} \quad (4.7)$$

where  $K$  is the crystallite shape factor (0.9 for spherical crystals),  $\lambda$  the wavelength of the source and  $B$  the  $2\theta$  FWHM, corrected for instrumental broadening as described above.

### 4.3 Optical conductivity/Integrating sphere

Transmission measurements were performed with an integrating sphere set-up, shown in Fig. 4.5. This contains a laser-driven unpolarized white light source (*Energetiq LDLS*), fibercoupled in a  $\text{NA} = 0.12$  fiber. After passing an achromatic lens (focal length=40 mm), light is

transmitted through the sample which is taped on a sample holder in front of the integrating sphere (*LabSphere*). The beam position on the sample can be changed by moving the xyz-stage on which the sample holder is mounted. Light is scattered inside the sphere and becomes spectrally homogenized so that a representative fraction of the full signal is sampled by fiber-coupling (NA = 0.22, diameter=105  $\mu\text{m}$ ) into a spectrometer (*Acton SpectraPro2300i*). The spectra recording is done with a CCD camera (*Princeton Instruments PIXIS 400*) and a grating (150 grooves/mm, blazed wavelength=500 nm) which is set to a center wavelength of 700 nm. This is controlled with the measurement software *WinSpec/32* (version 2.5).

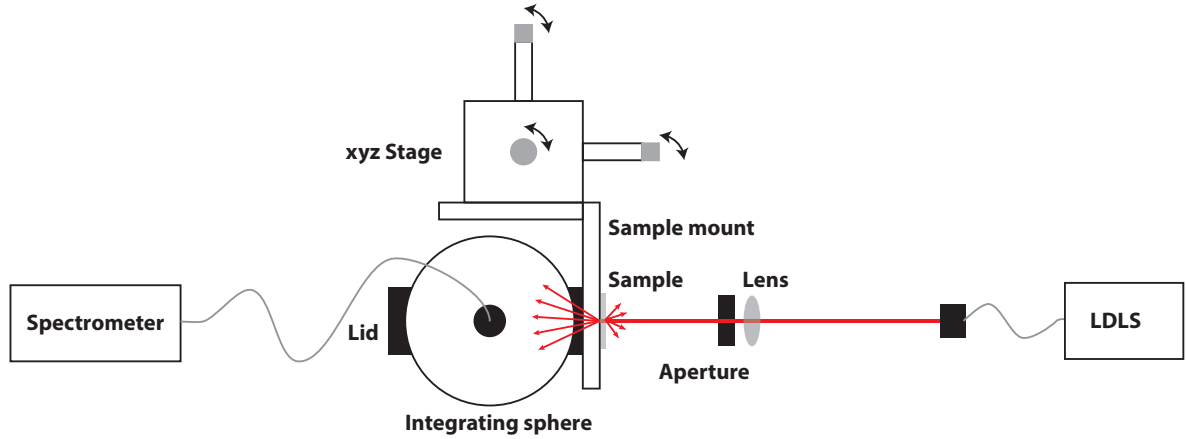


**Figure 4.5:** Optical setup consisting of a LDLS whose signal is fiber-coupled and passes a lens and an aperture, then is transmitted through a sample in front of an integrating sphere from which a homogenized signal is fiber-coupled into a spectrometer. Sample movements are performed with aid of the xyz-stage connected to the sample mount.

Ten spectra, each with a 4 s integration time were taken in the center of each array<sup>3</sup> 15 arrays were measured on each sample. The spectra were corrected for the dark current by subtracting it. Normalization was achieved through division by the signal of a bare borofloat glass wafer, subtracted of dark current. This procedure accounts for reflection losses from the substrate, thereby the actual transmission through the networks is obtained.

#### 4.4 Electrical conductivity/Four-point probing

Four-point probing enables measuring the sheet resistance of a film exclusive of the resistance of the contact pads, which is low compared to that of the networks, and the probes themselves which have resistances on the order of the network. This technique makes use of the property of the internal resistance of the voltage measure unit being orders of magnitude higher than that of the probes and the sample. This allows to approximate the resistance of the sample  $R_{\text{sample}}$  by the voltage drop over the voltage measure unit  $U_V$  and the current  $I$  passing through the whole system.

$$R_{\text{sample}} = \frac{U_V}{I} \quad (4.8)$$

The set-up consists of two outer force probes  $F_H$ ,  $F_L$  through which a current is sent (from high (H) to low (L) force) and two inner sense probes  $S_H$ ,  $S_L$  that measure the corresponding

<sup>3</sup>Additional test measurements on a different location showed a deviation of  $\approx 1\%$ . This suggests that measuring the center suffices, especially as it is known from SEM images that all fields are expected to be defect-free in the center.

voltage drop across the network. All probes are connected to a source measure unit (*Agilent B2902A*), see Fig. 4.6 and with the *Agilent quick I/V* software in voltage mode and a direct current ranging from 0.01 to 0.1 mA, I-V curves are recorded over two loops. The sheet resistance then corresponds to the slope of the V-I curve.

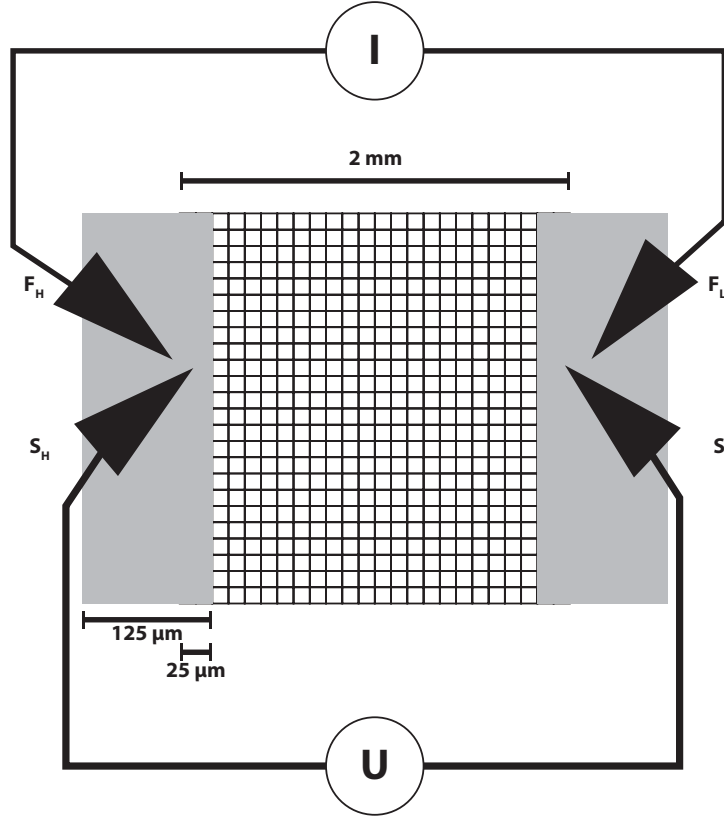


**Figure 4.6:** Schematic of a four-point-probe measurement on a network connected by contact pads on both sides. The outer probes are connected to a current source measure unit and the two inner probes measure the voltage drop across the network which is detected by a source measure unit. The dimensions of the contact pads are not proportionate to the network for better clarity.

## 4.5 Height/Atomic force microscopy

Atomic force microscopy (AFM) was employed to record height profiles of each sample. AFM works by scanning a surface with a piezo-driven tip mounted to a cantilever. The force between tip and sample displaces the cantilever when it approaches the surface and is translated into an electric signal. In tapping mode a constant frequency near the cantilever's resonance frequency and amplitude are chosen. When forces due to surface proximity change these, the height of the tip is adjusted to recover the set frequency and amplitude. This mode is preferred for measurements in atmosphere where liquid can be present on the surface which prohibits contact between tip and sample.

On each sample two different network arrays were investigated and the scan length was chosen to pass four nanowires in scan direction and five perpendicular to it (see Fig. 4.7a). Tapping frequencies between 0.502Hz and 0.749Hz were used. Height profiles were extracted using the software *Gwyddion* [18] along the marked red arrows. Fig. 4.7b shows the profile of the solid line. Each array height was calculated as the average peak height of all four extracted profiles.

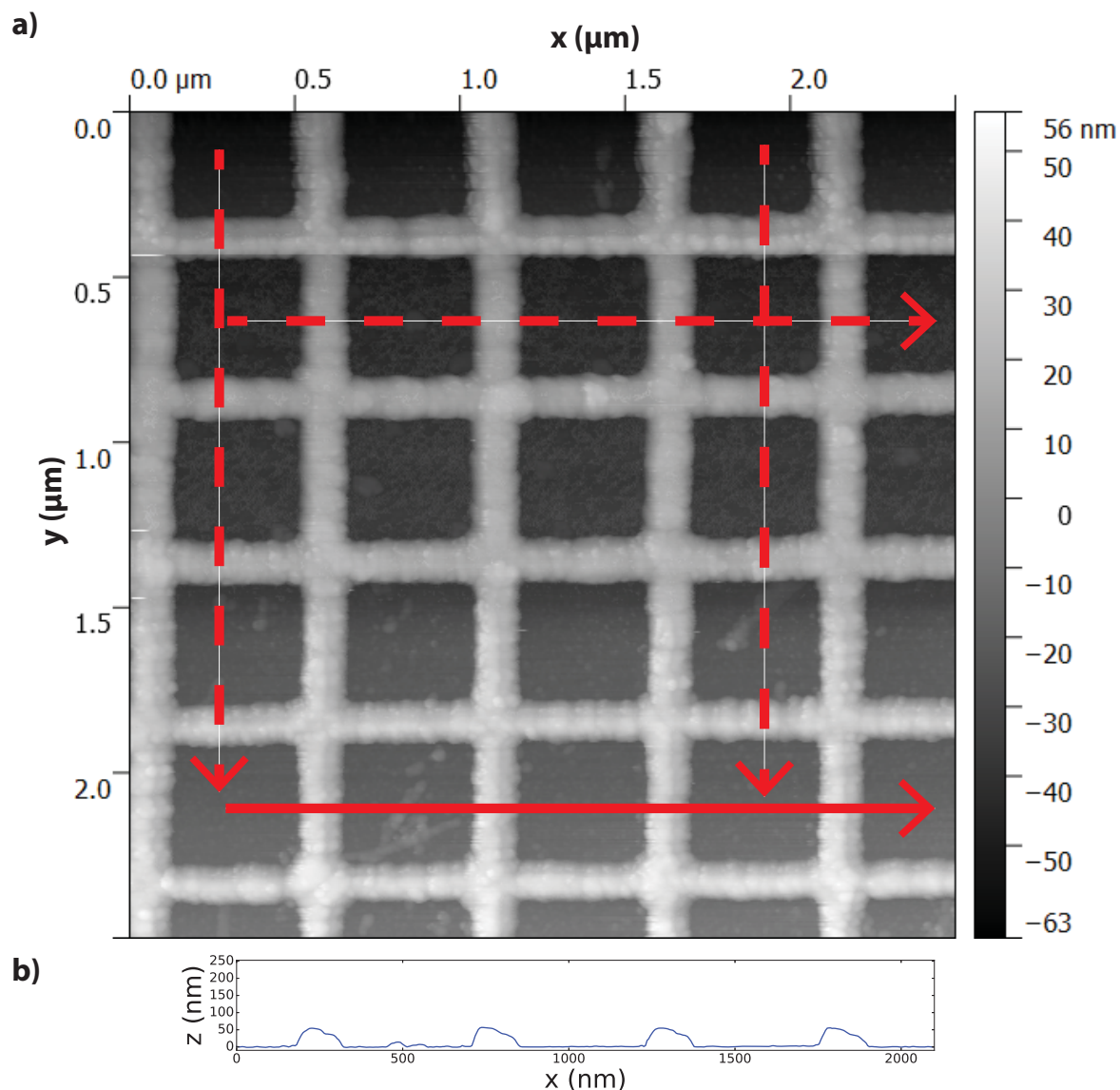


**Figure 4.7:** a) AFM scan of a network with pitch=500 nm. Height profiles were extracted along the red arrows. b) Height profile extracted along the solid line showing homogeneous heights of 56 nm.

The asymmetric peak shape observed in Fig. 4.7 could originate from the angle of incident Ag atoms during evaporation as a result of the evaporation chamber geometry as shown in Fig. 3.2.

---

## 5 Results

First, the results of the characterization methods are presented and further used to assess the opto-electrical performance of the NW networks.

### 5.1 Height

For the four samples evaporated at slower rates of 1 Å/s and 8 Å/s, average Ag heights between 52.5 nm and 56.5 nm were found which is in agreement with the previous calibration of the thermal evaporator. For five samples the deviation between the two locations was at most 6 nm. The Ag sample evaporated at the highest rate (effectively 15.4 Å/s) displays an elevated average height of 57.0 nm which indicates difficulties in controlling the exact height because of a less stable rate and a less reliable monitoring as the quartz crystal used as a reference is already covered due to the previous depositions. Reaction time plays a more important role at high rates, too, as one second already corresponds to an error of almost 2 nm. The recorded AFM spectra indicate a lack of homogeneity for high evaporation rates. In the Ge/Ag sample with the highest evaporation rate an average height of 53.5 nm was found for a network with  $\Lambda = 500$  nm whereas on a different network with  $\Lambda = 1000$  nm 71.5 nm was measured. Note that these networks lie only  $\approx 13$  mm apart. To account for this inhomogeneity, the average thickness was considered in calculations and simulations for all arrays on the same sample.

### 5.2 Grain size

From XRD measurements on flat Ag films (50 nm) on a 1 nm Ge seed layer which were evaporated at similar vacuum conditions as the samples ( $6.2 \cdot 10^{-7}$  mbar), a strong correlation between evaporation rate and grain size was found (Fig. 5.1a). The average grain sizes increase steadily with evaporation rate from 32.2 nm at 23 Å/s to 74.4 nm at 156 Å/s.

For the nanowire networks, the most noticeable feature is the different range in which grain sizes were found for the Ge/Ag samples, compared to Ag networks. The average grain sizes were between 28.4 nm and 40.4 nm for the former and 30.3 nm and 77.8 nm for the latter (Fig. 5.1b). The increasing trend with evaporation rate was only observed for the pure Ag samples. The Ge seeded samples show a decreasing grain size after an effective deposition rate  $> 8$  Å/s. However, the differences are small and likely lie within the measurement error of the XRD method. For the flat references on glass substrates that were co-evaporated with the nanowire networks, the Ge/Ag films show an increasing grain size with evaporation rate and the grain sizes deviate from the ones measured for the networks (Fig. 5.1c). In the samples without germanium the grain sizes found for the glass references show no clear trend in contrast to the NW networks and references and networks differ between 20 and 33 nm (Fig. 5.1d).



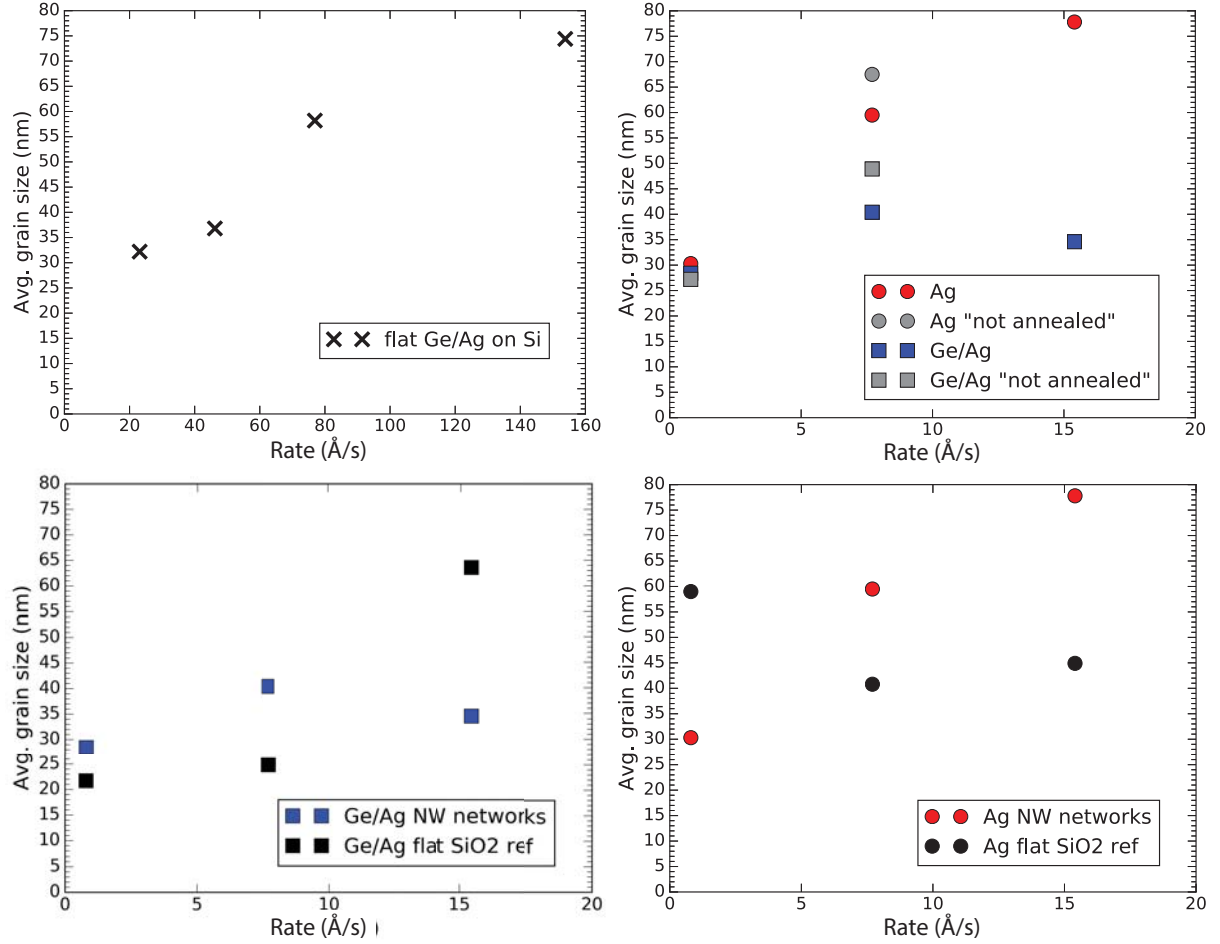


**Figure 5.1:** Average grain sizes extracted from XRD spectra as a function of effective evaporation rate for a) flat Ge/Ag on silicon, b) NW networks without (circles) and with (squares) a Ge seed layer for ascending (red, blue) and descending (grey) evaporation rates, c) NW networks with Ge layer (blue squares) and co-evaporated flat references on glass (black squares), d) Ag NW networks without Ge layer (red circles) and co-evaporated flat references on glass (black circles). Note the difference in x-axis between a) and the others as these samples were evaporated in a separate run.

At high evaporation rates the applied current is high which leads to more dissipated power. This is expected to translate to a rise in temperature which means the previously evaporated samples can become annealed during the evaporation of the last samples. Annealing even at temperatures well below the melting temperature of silver can increase the nanowire's grain size [9]. For a comparison, measured grain sizes of another batch of samples that was etched differently but evaporated in very similar conditions and at the same rates but in descending order (from high rate to low rate), hence labeled 'not annealed', are included in Fig. 5.1b. For a slow evaporation, the non-annealed sample shows a very similar grain size as the others. For a higher evaporation rate however a 8 nm larger average grain size was found in the non-annealed networks, independent of the presence of a Ge seed layer. This suggests that annealing did not take place and gives evidence on the error of the XRD method as a deviation of almost 10 nm can be observed for samples that are expected to have very similar grain structure due to almost identical processing.

The XRD measurement on the network on silicon of Ag evaporated at a rate of 1.5 Å/s and with a Ge seed layer (shown in Fig. 4.1) yields an average grain size of 21.2 nm. Based on SEM distance measurements the size of visible and thus above-average large grains was

between 15 nm and 30 nm. As XRD gives merely an average and assuming grains growing from the bottom all to the top, this means lateral grain dimensions are expected to be smaller than this measured value. This is in accordance with the large number of small grains obtained from SEM images.

### 5.3 Opto-electrical

To assess the results of four-point probe experiments, the measured sheet resistances are plotted against the ratio of width and pitch (Fig. 5.2) as determined from SEM images. This corresponds to the metal filling fraction. Fig. 5.2a shows the Ag network samples and b the Ge/Ag networks. The error bars account for uncertainty in width arising from SEM images and possible oxidation and is assumed to be  $\pm 5$  nm. The error of pitch is neglected.

The Mayadas-Shatzkes model is employed to fit theoretical values of resistivity according to Eq. 2.5, based on the parameters used in [9]. From this, sheet resistances are determined with Eq. 2.2 and actual dimensions found from SEM and AFM, shown as solid lines in Fig. 5.2. Because the grain boundary reflectivity  $R$  changes with processing condition [19],  $R$  was used as a fit parameter. To account for uncertainty in grain size, the resistances are re-calculated with the fitted reflectivity parameter assuming the error in  $L$  is  $\pm 10$  nm, resulting in lower and upper bounds (dashed lines). The fitted  $R$  values are similar to values found in literature [9], [20] which confirms the model. However, these fits do not follow the expectation of smaller  $R$  with larger average grain size as in ref. [20]. Contrarily, the largest reflection coefficient is found for the largest  $L$  (yellow curve in Fig. 5.2a). For comparison, the Mayadas-Shatzkes calculation was re-done with a constant  $R$  of 0.57 for all samples as suggested in [9]. This was found to describe some of the measured data poorly.

Most remarkable is that the pure Ag networks show resistances almost half that of the Ge/Ag (Fig. 5.2a,b) which is in accordance to the generally larger grain sizes found in Ch. 5.2.

For the Ag samples there is a correlation of lower sheet resistance with larger grain size but the spread of resistances for different grain sizes is relatively low. For the Ge/Ag networks the sheet resistance decreases with higher evaporation rate. This rate is a more significant benchmark than the grain size in these networks as the differences in grain sizes between samples is within the error of the XRD method.

AFM measurements showed differences in height between the samples which can influence their sheet resistances. For a more fair comparison between the samples, the measured sheet resistances are converted to resistivities (according to Eq. 2.2) which excludes geometrical influences and is shown in Fig. 5.3 together with fitted resistivity values (solid lines) and the deviations due to uncertainty in grain size (dashed lines). Error in y-axis is due to errors in height and width, whereas the x-error is the same as in Fig. 5.2. The height error of  $\pm 6$  nm was assumed from the common deviation within the same sample found from AFM. In Fig. 5.3a it is observed that the Ag networks (circles) first show a reduction in resistivity from  $5.4 \cdot 10^{-8} \Omega\text{m}$  to  $4.9 \cdot 10^{-8} \Omega\text{m}$  but then a repeated increase to  $5.6 \cdot 10^{-8} \Omega\text{m}$  despite an increase in average grain size by 10 nm. In this regime the average grain size exceeds the wire dimensions along the height and width ( $w_{\min} = 50$  nm). The rise in resistivity could hence originate from spatial confinement. Fig. 5.3b shows that in the Ge/Ag networks (squares) resistivity decreases with increasing evaporation rate.

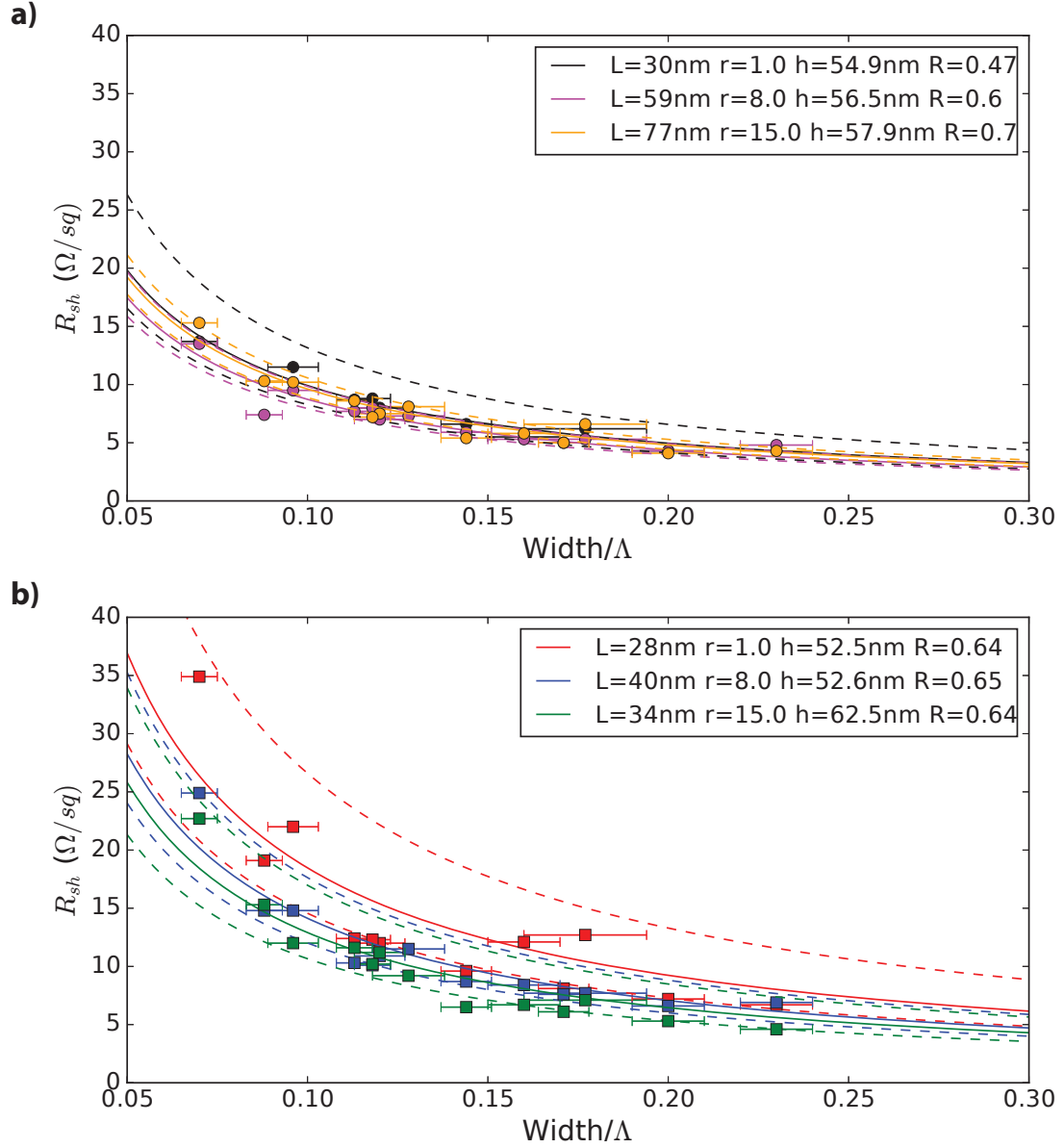


**Figure 5.2:** Measured sheet resistance on various arrays on each sample over the respective ratio of width and pitch for a) pure Ag networks and b) Ge/Ag networks. The lines are calculated with the Mayadas-Shatzkes model, solid without error, dashed assuming error in grain size specified in the text. Labels indicate average grain size ( $L$ ), evaporation rate ( $r$ ), average network height ( $h$ ) and the obtained fit parameter of reflection coefficient ( $R$ ).

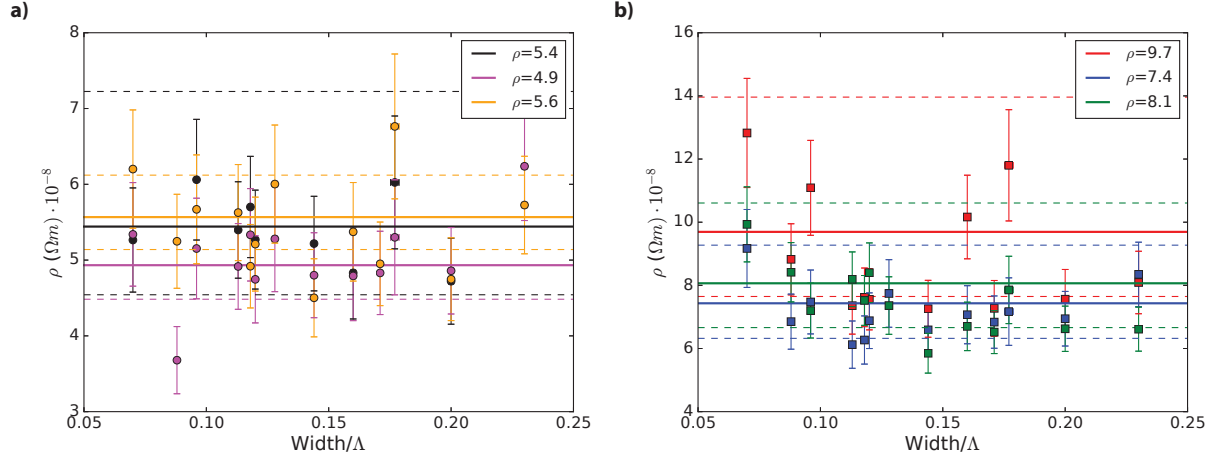


**Figure 5.3:** Calculated resistivities from the measured resistances and fitted resistivities a) for Ag networks and b) for Ge/Ag networks. Errors are due to uncertainties in wire height and width. The dashed lines are errors of the fit that stem from grain size uncertainty. Same color code as in Fig. 5.2 is employed.

An example of an optical spectra obtained is shown in Fig. 5.4. All curves were measured on the same network on the respective samples a) without and b) with Ge seed layer. As the difference in height is  $< 10$  nm which does not have a large impact on the optical properties, these samples mainly differ in their evaporation rate and grain size. The spectra show a slight blue-shift of SPP of maximum 10 nm for Ag (Fig. 5.4a) and 23 nm for Ge/Ag (at  $\lambda \approx 820$  nm with increasing evaporation rate but overall are very similar. The pure Ag networks with slower rate and smaller grain size show a 1% higher transmission when weighted with the AM1.5 spectrum Fig. 5.4a compared to the samples with larger rates and grains. In the Ge/Ag samples this value also reduces by 1 – 2% by increasing the evaporation rate (Fig. 5.4b) which does not reflect larger grains (see Fig. 5.1b). The maximum reduction in AM1.5-weighted transmission found between the highest evaporation rate (15 Å) and the slowest (1 Å) is 4% for the Ge/Ag samples and 3% for the pure Ag networks. The shifts in SPP resonance from the measured spectra in Fig. 5.4 amount to 10 nm for the Ag networks and 20 nm for Ge/Ag. One explanation for this reduction could be the greater heights of the samples with the highest rate. From Fig. 2.3 it is known that the SPP shifts by  $\approx 30$  nm for a height difference of 10 nm. This means the observed shifts could be explained by the deviation in heights between the samples. Also the simulated AM1.5 transmission reduces by 1% with this height difference. Another contribution to the different optical performance could be surface roughness due to different evaporation rates.

The average difference in AM1.5-averaged measured transmission between Ge/Ag and Ag NW networks evaporated at the same rate is 3% in favor of pure Ag, obtained from the data shown in Table 4.

|       |       | r=1         |             |             | r=8         |             |             | r=15        |             |             |
|-------|-------|-------------|-------------|-------------|-------------|-------------|-------------|-------------|-------------|-------------|
| pitch | width | Ag          | Ge/Ag       | $\Delta T$  | Ag          | Ge/Ag       | $\Delta T$  | Ag          | Ge/Ag       | $\Delta T$  |
| 300   | 53    | 0.79        | 0.76        | 0.03        | 0.77        | 0.77        | 0.00        | 0.78        | 0.76        | 0.02        |
| 500   | 64    | 0.87        | 0.85        | 0.02        | 0.86        | 0.83        | 0.03        | 0.86        | 0.82        | 0.04        |
| 700   | 65    | 0.85        |             |             | 0.84        | 0.81        | 0.03        | 0.84        | 0.80        | 0.04        |
| 1000  | 70    | 0.90        |             |             | 0.88        | 0.87        | 0.01        | 0.89        | 0.90        | 0.01        |
| 500   | 80    | 0.79        | 0.76        | 0.03        | 0.78        | 0.75        | 0.03        | 0.79        | 0.74        | 0.05        |
| 700   | 84    | 0.79        | 0.76        | 0.03        | 0.78        | 0.73        | 0.05        | 0.77        | 0.72        | 0.05        |
| 1000  | 88    |             |             |             | 0.84        | 0.81        | 0.03        | 0.83        | 0.81        | 0.02        |
| 500   | 100   | 0.71        | 0.66        | 0.05        | 0.71        | 0.65        | 0.06        | 0.71        | 0.65        | 0.06        |
| 700   | 101   | 0.72        |             |             | 0.70        | 0.67        | 0.03        |             |             |             |
| 1000  | 113   | 0.76        |             |             | 0.75        | 0.72        | 0.03        | 0.75        | 0.72        | 0.03        |
| 1000  | 120   | 0.75        |             |             | 0.73        | 0.69        | 0.04        | 0.72        | 0.69        | 0.03        |
|       | avg   | <b>0.79</b> | <b>0.76</b> | <b>0.03</b> | <b>0.79</b> | <b>0.75</b> | <b>0.04</b> | <b>0.79</b> | <b>0.76</b> | <b>0.03</b> |

**Table 4:** AM1.5-weighted transmission data presented by rate and material showing the average in each Ag and Ge/Ag network and the difference  $\Delta T$  between the materials at the same rate.

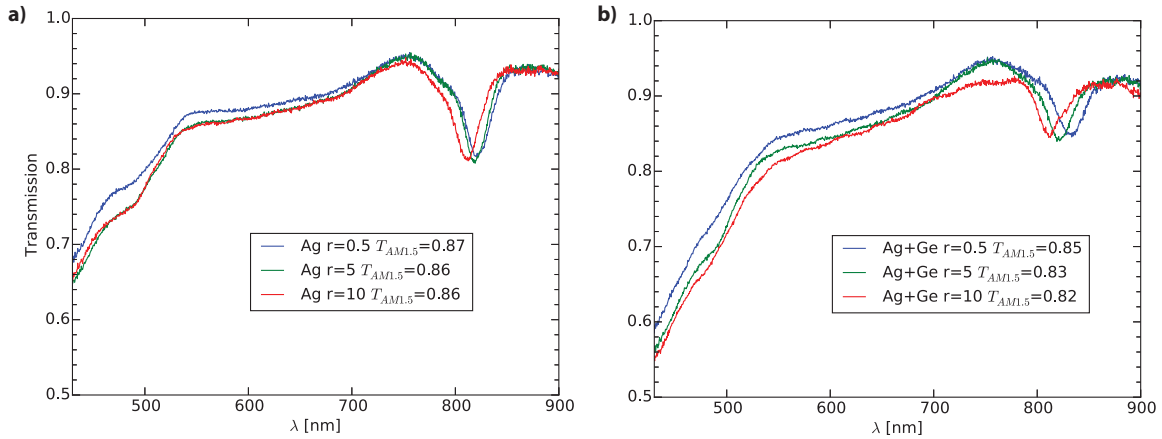


**Figure 5.4:** Measured transmission spectra on a network with pitch of 500 nm a) on Ag evaporated at 0.8 Å/s and an average grain size of 30.3 nm (blue), on Ag evaporated at 7.7 Å/s with an average grain size of 59.5 nm (green) and on Ag evaporated at 15 Å/s and a grain size of 77.8 nm and b) on Ge/Ag evaporated at 0.8 Å/s (blue), 7.7 Å/s (green) and 15 Å/s with grain sizes 28.4 nm, 40.4 nm and 34.6 nm respectively.

To display the typical trade-off in TCEs, the AM1.5-averaged transmission is displayed over the measured sheet resistances in Fig. 5.5. This shows that our networks have small resistances ( $< 20 \Omega/\text{sq}$ ) and AM1.5-weighted transmissions of 80 – 90% for pure Ag networks and 75 – 90% in Ge/Ag networks are observed which indicates their suitability as TCEs.

For comparison, theoretical values obtained from FDTD simulations of rounded wires with a radius of curvature of  $0.3 \cdot w$  and actual dimensions found from microscopy and sheet resistances calculated with the Mayadas-Shatzkes model are included (crosses). These indicate that our networks are in good agreement with expectations from theory.

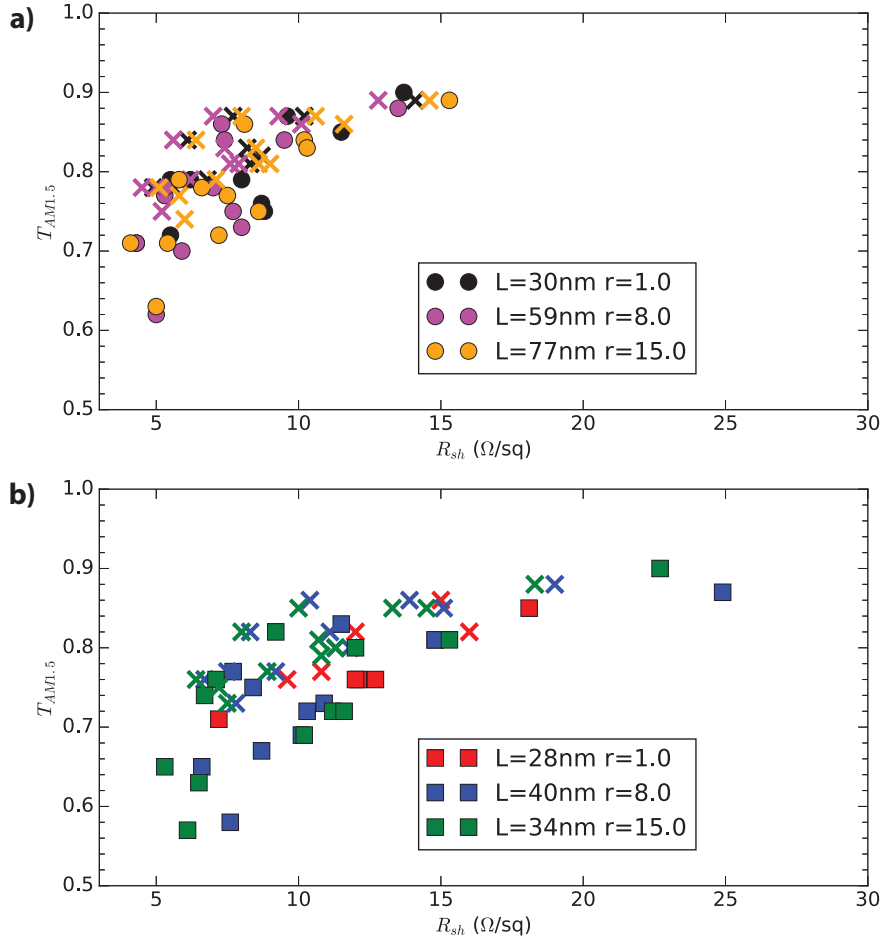


**Figure 5.5:** Trade-off between AM1.5-weighted Transmission and measured sheet resistances in a) Ag networks and b) Ge/Ag networks. Theoretical values obtained from FDTD simulations and Mayadas-Shatzkes model (crosses) are included for comparison.

ITO is not included in Fig. 5.5 because it lies outside the displayed range of sheet resistances.

## 5.4 Insights into substrate-conformal imprint lithography

To calibrate the parameters of the imprint tool and to investigate the behavior of the UV-curable solgel, several test imprints were done. SEM images and focused ion beam (FIB) cross sections were employed to monitor the effect of every processing step.

The general trade-off is to achieve a breakthrough etch on a large number of networks and at the same time do not increase the wire widths by over-etching.

The imprint parameters determined for use in the SCIL tool as a result of the tests presented in this chapter were shown previously in Table 3.

### 5.4.1 Parameters for sample fabrication, calibration of tool & UV solgel

The process delay and post process delay, which is the time when substrate and stamp are already/still in contact before/after the exposure, was varied (see Fig. 5.6). No influence on wire dimensions or quality was observed and 60 s each was chosen to guarantee solgel flow around all stamp features.

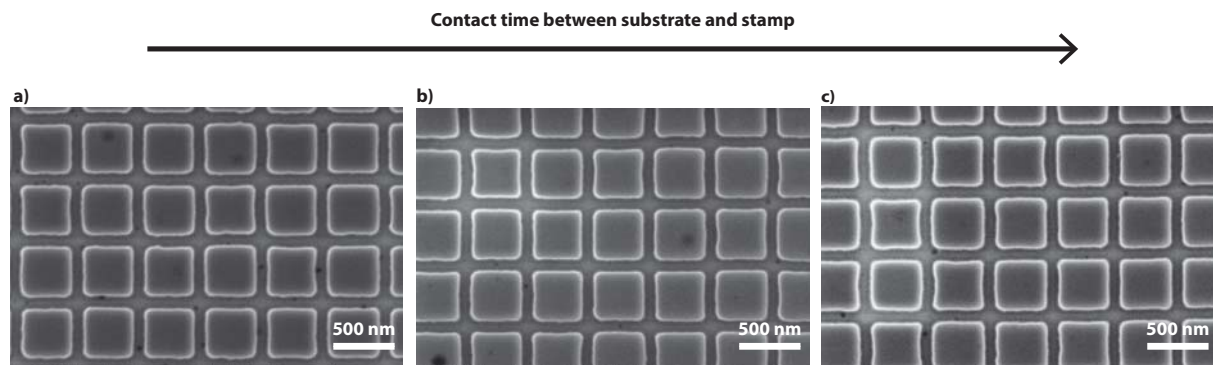


**Figure 5.6:** SEM images of imprinted UV solgel using different pre- and post-exposure delay times, a) pre: 30 s, post: 10 s, b) 30 s each and c) 60 s each. Exposure time was 120 s for all.

FIB cross sections of this imprint show deviations in solgel thickness between two different locations on the stamp to be up to 50 nm from 70 – 120 nm, and residual solgel ranging from 18 nm (at  $\Lambda = 1000$  nm) to 44 nm (at  $\Lambda = 500$  nm).

Cross section images of PMMA and solgel on silicon were taken after only imprint (Fig. 5.7a and b), compared to additional solgel etch (Fig. 5.7c and d) and to after a subsequent 2 min oxygen etch (Fig. 5.7e and f). Inhomogeneous PMMA thicknesses ranging from 120 – 220 nm were obtained and PMMA swelling (around trenches in Fig. 5.7e and f) was observed. This is ascribed to solvents in the solgel becoming absorbed by the PMMA, thereby enlarging the bottom trench width from 63 nm to 99 nm (see Fig. 5.7d and f). To prevent this swelling, post-baking the solgel for 15 min at 70°C after imprint was employed (see Fig. 5.8).

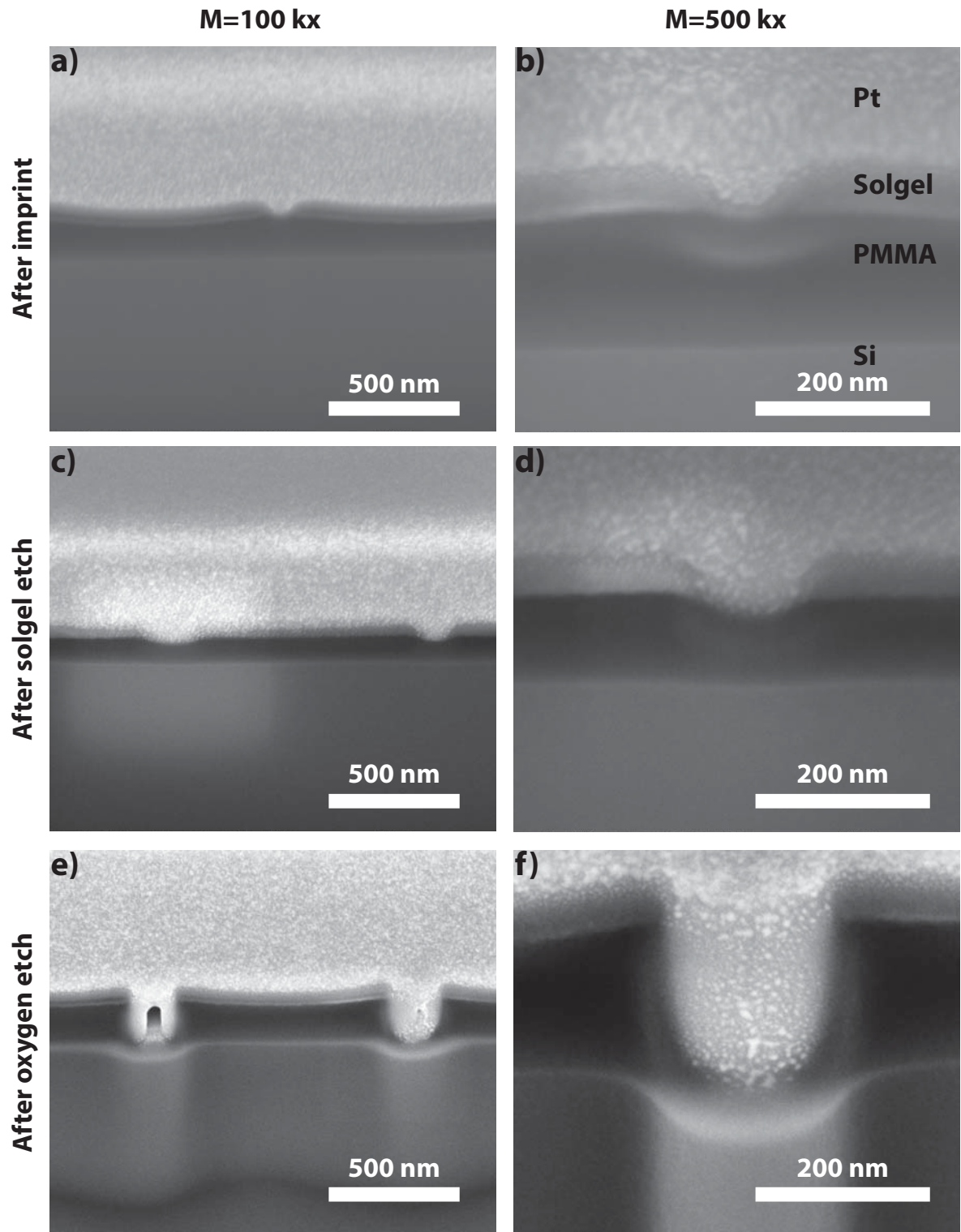


**Figure 5.7:** FIB cross sections of PMMA and UV solgel on silicon, a) and b) after imprint, c) and d) after solgel etch, e) and f) after additional oxygen etch showing PMMA swelling. b), d), f) are (the respective) high-magnification images (M=500 kx) of samples shown in a), c), e) (M=100 kx). The Platinum (Pt) layer was deposited for cleaner milling and better image quality.

Further the duration of the oxygen etch was optimized. FIB cross sections were taken on different network arrays depicted in Fig. 5.8. They show that halving the etch time to 6 minutes (Fig. 5.8a and b) already exposes the substrate and forms an undercut. This undercut



is much more pronounced for the smaller-pitched network. Compared to this, the  $\Lambda = 1000$  nm trench show rather straight walls both after 6 min (Fig. 5.8a) and 12 min (Fig. 5.8c) etch. Simultaneously Fig. 5.8 illustrates less broadening due to some isotropy in the oxygen etch. The measured trench width for the sample shown in Fig. 5.8a is 14 nm less than when etched for 12 minutes (Fig. 5.8c). This difference is barely larger than the combined SEM measurement error and the general deviation between samples, so no significant influence can be ascribed to etch time. This shows the sufficient anisotropy of the employed etcher (*Oxford PlasmaLab System 100*) and recipe. The lift-off worked equally well on all networks independent of the pitch.

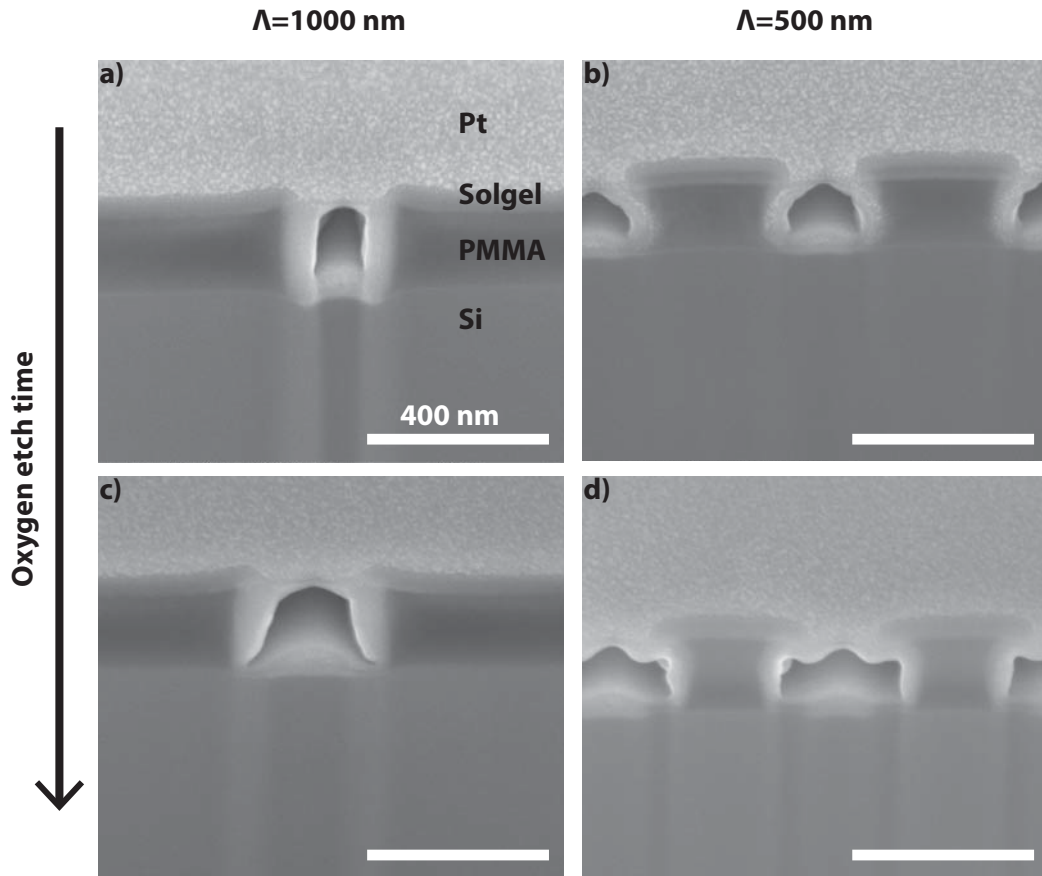


**Figure 5.8:** FIB cross sections of UV solgel and PMMA after post-baking for 15 min, solgel etch and a), b) 6 minutes and c), d) 12 minutes oxygen etch for networks with a pitch of 1000 nm (a), c)) and 500 nm (b), d)). The scale bar is 400 nm in each image.

#### 5.4.2 Master & stamp fabrication

Advances were made to replicate a master from a SCIL-stamp imprint. This can be done by spin-coating and imprinting only a solgel layer on a silicon wafer, transferring the imprint into silicon by etching and using this as a master mold for the PDMS layers.

The solgel spin-rotation was found to be a very important parameter as it directly affects film thickness. Fig. 5.9a-f show SEM images of hand-imprinted (homemade) solgel on silicon wafers for different spin-rotations from 600 – 1000 rpm (thicknesses obtained from profilometer are 108 nm, 95 nm and 83 nm, respectively). This shows how deformations resulting from imprinting in a too thin layer become less pronounced by reducing the spin-rotation. This can be explained by the Young's modulus. The used spinning recipe was developed for

having a PMMA layer with an Young's modulus of 1.8 – 3.1 GPa [21] between solgel and silicon substrate which has a modulus of (170 GPa [22]). Repeated imprinting into a too thin layer on a rigid substrate may have caused permanent deformation and rendered the stamp unusable. Therefore an own master could not be fabricated and instead an elsewhere produced master and stamp were used. Due to time constraints, reproduction of this master and stamp could not be finished in the scope of this work. However, the etch recipe to make a stamp was developed (see Table 5) and optimized for 70 nm deep trenches but not checked for lateral trench dimensions. To check this in the future, it is useful to note that it was observed that evaporated metal wire dimensions are 30 nm narrower than suggested by trench widths measured with SEM and FIB.

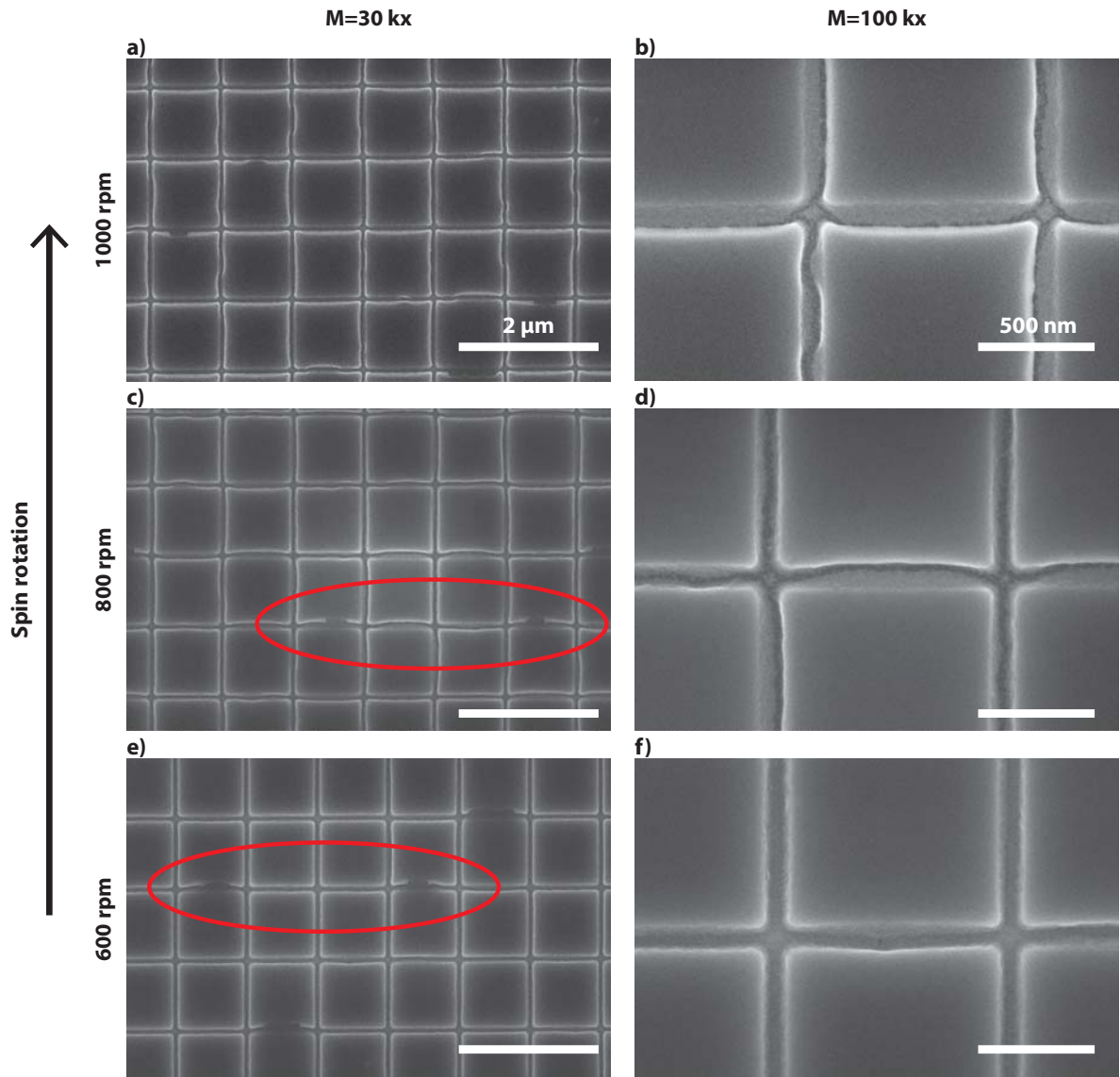


**Figure 5.9:** SEM images of imprinted solgel spin-coated at a rotation of a), b) 1000 rpm, c), d) 800 rpm, e), f) 600 rpm, magnified 30 kx (a), c), e), scale bar=2  $\mu\text{m}$ ) and 100 kx (b), d) and f), scale bar=500 nm.

| Solgel etch         |                |
|---------------------|----------------|
| Pressure            | 15 mTorr       |
| HF                  | 67 W           |
| Helium              | 10             |
| DC                  | 232            |
| Cryo                | 20°C           |
| Ar                  | 25 sccm        |
| CHF <sub>3</sub>    | 25 sccm        |
| resulting etch rate | 10 – 20 nm/min |
| time                | 3 min          |
| pump-out for 1 min  |                |
| Si etch             |                |
| Pressure            | 7 mTorr        |
| HF                  | 30 W           |
| Helium              | 10             |
| DC                  | 140            |
| Cryo                | 20°C           |
| HBr                 | 48 sccm        |
| O <sub>2</sub>      | 2 sccm         |
| resulting etch rate | 105 nm/min     |
| time                | 40 s           |

**Table 5:** Reactive ion etch recipe for a master with 70 nm deep trenches, consisting of a solgel etch, a chamber pump-out and a silicon etch.

---

## 6 Discussion

We found that grain size is a key parameter for the opto-electrical performance of NW networks. In particular the sheet resistance is determined by this parameter.

The direct correlation between fast metal deposition rate and large grain size was observed in Ag NW networks on glass and in flat Ge/Ag films on silicon. For Ge/Ag networks on glass the grain sizes obtained from XRD measurements all lie within the observed error of this measurement technique and therefore this trend can be neither verified nor contradicted for these samples.

The corresponding resistivities calculated with the Mayadas-Shatzkes model show an interesting feature: for the Ag network in which the average grain size exceeds wire height and minimum width by almost 30 nm, an increase in resistivity was found compared to the previous trend of reduced resistivity for larger grains. This indicates that confinement could play a role and an optimum grain size exists. For the Ge/Ag networks in which the largest average grain size is 40 nm however, the resistivity is steadily decreasing with faster evaporation. The grains in these networks are too small to experience a confinement which suggests that the optimum grain size and evaporation rate might not yet be reached for the Ge/Ag networks. In this thesis, Ag NW networks showed superior performance, both optically and electrically, compared to the Ge/Ag network samples. By employing the Mayadas-Shatzkes model, improved conductivity can be ascribed to larger average grain sizes in these samples. This benefit on conductivity is in contrast to a previous study [23] in which a thin layer of germanium between a native-oxidized Si wafer and evaporated Ag (rate 1 Å/s) was found to yield grain sizes and surface roughnesses of one order of magnitude lower than without germanium (10 nm compared to 100 nm and 0.6 nm compared to 6 nm, respectively). This general trend is in agreement with our results as our Ge/Ag samples also show average grain sizes smaller than pure Ag with a maximum difference of 39 nm. However, for the earlier reported Ge/Ag films the sheet resistance of 20 Ω/sq was only half that of pure Ag [23]. It is argued that irregularity and surface roughness of films grown without germanium lead to higher resistance which is traced back to discontinuous nucleation and voids in the film [23]. We find the grain size in Ag samples to be approximately twice that as in Ge/Ag, accompanied by a sheet resistance reduced by a factor of 2 for low metal filling fractions which are desired for high transmission. To investigate the necessity of including a Ge seed layer, for example for improved Ag adhesion, in the future stability tests such as scotch tape and bending should be performed on these networks. These results then need to be weighted against opto-electrical losses.

For the investigated Ag NW networks no reduction in optical losses was observed with higher evaporation rate, contrary to Ag films explored in [11]. We rather see the opposite behavior of a slight decrease in transmission for faster evaporation and larger grain sizes. This could be explained with deviations in height between the samples. Increased roughness and hence decreased specular reflection resulting from faster evaporation could also contribute to this. In a previous study it was found that regular surface roughness can explain a red-shift of a plasmonic resonance as the plasmon accommodates to this [8]. This would suggest there is more regular surface roughness present in the samples evaporated at slower deposition rates compared to irregular surface roughness for fast rates.

To further investigate this, surface roughness could be quantified with a stochastic analysis of AFM data.

Grain sizes stated in this thesis should not be taken as an absolute value but rather serve

---

as a qualitative comparison as in the analysis of XRD spectra the strain contribution was not taken into account. Transmission electron microscopy could further be used to analyze grain structures and quantify grain sizes. The XRD signal could then be deconvoluted to indicate the strain contribution and calculate a more significant absolute grain size.

For an 80 nm thick sputtered layer of ITO a sheet resistance of  $58.2 \Omega/\text{sq}$  accompanied by an average transmission of 88% was found [6]. This is significantly more resistive than the networks presented in this thesis. Another comparison can be drawn to solution-processed networks reported in [9]. Our fabricated wires exceed the solution-processed in average transmission for a given sheet resistance. For  $R_{\text{sh}} = 8 \Omega/\text{sq}$  the Transmission in solution-grown wires amounts to 79% whereas in our networks it reaches 87%. The largest grain size obtained in a Ag network was 78 nm which exceeds the solution-grown by 18 nm. For solution-grown wires sheet resistances below  $3 \Omega/\text{sq}$  are reported. This beats our most conductive network which showed  $R_{\text{sh}} = 4.1 \Omega/\text{sq}$ . Comparing the electric performance of our network resistivities to bulk Ag, shows resistivities of 3 to 6 times that of  $\rho_{\text{bulk}}$ .

A possible effect in these networks which could limit their performance when used as TCEs is electromigration which describes a mass transfer due to collisions between moving electrons and activated ions [24]. This can lead to circuit failure and can be an issue in these networks due to the large number of grain boundaries and material interfaces.

---

## 7 Conclusion & Outlook

High-quality Ag NW networks have been fabricated using a scalable technique. The networks show significantly reduced sheet resistances compared to ITO of up to one order of magnitude whilst optical transmission is comparable. Our networks show an improved trade-off between optical and electrical performance compared to previous studies on solution-grown Ag networks [9].

Our most conductive network has a sheet resistance of  $4.1 \Omega/\text{sq}$ , which is lower than  $6.5 \Omega/\text{sq}$  reported before for evaporated networks [6], and the most transparent network has an AM1.5-averaged transmission of 90%. Grain sizes comparable to solution-grown Ag wires [9] were obtained by increasing the effective evaporation rate to  $15 \text{ \AA}/\text{s}$ .

For Ag NW networks a correlation of fast evaporation rate and large grain size was found. Investigating more samples evaporated at intermediate rates might confirm this trend also for Ge/Ag wires.

With sample fabrication performed in the SCIL tooling and by employing a fast-curing resist, a high throughput was achieved which shows this technique's potential of becoming commercially used in the future.

This study can pave the way for a solar cell design including optimized metal nanowire networks which perform at their theoretical limit which can lead to an increase in solar cell efficiency.

Further studies are necessary to confirm the reproducibility and assess an optimum grain size and possibly processing recipe which might be determined by a saturation effect due to average grains larger than the wire dimensions indicated by the results of this thesis.

Future studies should investigate long-term performance, effects of encapsulation (for example with  $\text{SiN}_x$ ) and include stability tests such as scratching and bending to further assess the potential of these networks to replace ITO. Aluminum and copper wires as cheaper alternatives should be investigated, too in the context of optimized grain structure.

---

## References

- [1] Huiyong Liu, V. Avrutin, N. Izyumskaya, Ü Özgür, and H. Morkoç. Transparent conducting oxides for electrode applications in light emitting and absorbing devices. *Superlattices and Microstructures*, 48(5):458–484, 2010.
- [2] Dhriti Sundar Ghosh. *Ultrathin Metal Transparent Electrodes for the Optoelectronics Industry*. Springer Science & Business Media, 2013.
- [3] Vivian E. Ferry, Marc A. Verschuuren, M. Claire Van Lare, Ruud E. I. Schropp, Harry A. Atwater, and Albert Polman. Optimized spatial correlations for broadband light trapping nanopatterns in high efficiency ultrathin film a-Si:H solar cells. *Nano Letters*, 11(10):4239–4245, 2011.
- [4] Z.C. Holman, A. Descoeudres, L. Barraud, F.Z. Fernandez, J.P. Seif, S. De Wolf, and C. Ballif. Current Losses at the Front of Silicon Heterojunction Solar Cells. *IEEE Journal of Photovoltaics*, 2(1):7–15, 2012.
- [5] Mark W Knight and Jorik Van De Groep. Soft Imprinted Ag Nanowire Hybrid Electrodes on Silicon Heterojunction Solar Cells. *unpublished*, pages 1–20.
- [6] Jorik Van De Groep, Pierpaolo Spinelli, and Albert Polman. Transparent conducting silver nanowire networks. *Nano Letters*, 12(6):3138–3144, 2012.
- [7] A. F. Mayadas and M. Shatzkes. Electrical-resistivity model for polycrystalline films: The case of arbitrary reflection at external surfaces. *Physical Review B*, 1(4):1382–1389, 1970.
- [8] Andreas Trügler, Jean-Claude Tinguely, Joachim Krenn, Andreas Hohenau, and Ulrich Hohenester. Influence of surface roughness on the optical properties of plasmonic nanoparticles. *Physical Review B*, 83(8):081412, 2011.
- [9] Beniamino Sciacca, Jorik van de Groep, Albert Polman, and Erik C. Garnett. Solution-Grown Silver Nanowire Ordered Arrays as Transparent Electrodes. *Advanced Materials*, 2015.
- [10] Henry Levinstein. The Growth and Structure of Thin Metallic Films. *J. Appl. Phys*, 20:306–315, 1949.
- [11] Kevin M. McPeak, Sriharsha V. Jayanti, Stephan J. P. Kress, Stefan Meyer, Stelio Iotti, Aurelio Rossinelli, and David J. Norris. Plasmonic Films Can Easily Be Better: Rules and Recipes. *ACS Photonics*, 2(3):326–333, 2015.
- [12] M G Blaber, M D Arnold, and M J Ford. A review of the optical properties of alloys and intermetallics for plasmonics. *Journal of Physics: Condensed Matter*, 22(14):143201, 2010.
- [13] David Griffiths. *Introduction to Electrodynamics (3rd ed.)*. Prentice Hall, 1999.
- [14] Lumerical Solutions, Inc. <http://www.lumerical.com/tcad-products/fdtd/>.
- [15] Marcus Verschuuren. *Substrate Conformal Imprint Lithography for Nanophotonics*. Ph.D. thesis, Utrecht University, 2010.

- 
- [16] Bruker. D2 Phaser Prospekt. page 12.
- [17] P. Scherrer. Bestimmung der Grösse und der inneren Struktur von Kolloidteilchen mittels Röntgenstrahlen. *Nachr. Ges. Wiss. Göttingen*, 26:98–100, 1918.
- [18] Petr Nečas, David and Klapetek. Gwyddion: an open-source software for SPM data analysis. *Central European Journal of Physics*, 10(1):181–188, 2012.
- [19] N. Artunç, M. D. Bilge, and G. Utlu. The effects of grain boundary scattering on the electrical resistivity of single-layered silver and double-layered silver/chromium thin films. *Surface and Coatings Technology*, 201(19-20 SPEC. ISS.):8377–8381, 2007.
- [20] Kuo Ping Chen, Vladimir P. Drachev, Joshua D. Borneman, Alexander V. Kildishev, and Vladimir M. Shalaev. Drude relaxation rate in grained gold nanoantennas. *Nano Letters*, 10(3):916–922, 2010.
- [21] MIT Material Property Database, <http://www.mit.edu/~6.777/matprops/pmma.htm>.
- [22] Euan J Boyd and Deepak Uttamchandani. Measurement of the Anisotropy of Young’s Modulus in Single-Crystal Silicon. *Journal of Microelectromechanical Systems*, 21(1):243–249, 2012.
- [23] V. J. Logeeswaran, Nobuhiko P. Kobayashi, M. Saif Islam, Wei Wu, Pratik Chaturvedi, Nicholas X. Fang, Shih Yuan Wang, and R. Stanley Williams. Ultrasooth silver thin films deposited with a germanium nucleation layer. *Nano Letters*, 9(1):178–182, 2009.
- [24] P. S. Ho and T. Kwok. Electromigration in metals. *Rep. Prog. Phys.*, 52:301–348, 1989.